PREDICTION OF STRESSES IN RIGID AIRPORT PAVEMENTS CONSIDERING SLAB'S TEMPERATURE DIFFERENTIAL USING FINITE ELEMENT AND MACHINE LEARNING TECHNIQUES

ERICK DOUGLAS DE LUNA SANTOS

DISSERTAÇÃO DE MESTRADO EM ESTRUTURAS E CONSTRUÇÃO CIVIL
DEPARTAMENTO DE ENGENHARIA CIVIL E AMBIENTAL

FACULDADE DE TECNOLOGIA

UNIVERSIDADE DE BRASÍLIA

UNIVERSIDADE DE BRASÍLIA
FACULDADE DE TECNOLOGIA
DEPARTAMENTO DE ENGENHARIA CIVIL E AMBIENTAL

PREDICTION OF STRESSES IN RIGID AIRPORT PAVEMENTS CONSIDERING SLAB'S TEMPERATURE DIFFERENTIAL USING FINITE ELEMENT AND MACHINE LEARNING TECHNIQUES

ERICK DOUGLAS DE LUNA SANTOS

ORIENTADOR: Ph.D. FRANCISCO EVANGELISTA JUNIOR

DISSERTAÇÃO DE MESTRADO EM ESTRUTURAS E CONSTRUÇÃO CIVIL

PUBLICAÇÃO:
BRASÍLIA/DF – DEZEMBRO/2024

UNIVERSIDADE DE BRASÍLIA

FACULDADE DE TECNOLOGIA

DEPARTAMENTO DE ENGENHARIA CIVIL E AMBIENTAL

PREDICTION OF STRESSES IN RIGID AIRPORT PAVEMENTS CONSIDERING SLAB'S TEMPERATURE DIFFERENTIAL USING FINITE ELEMENT AND MACHINE LEARNING TECHNIQUES

ERICK DOUGLAS DE LUNA SANTOS

DISSERTAÇÃO DE MESTRADO SUBMETIDA AO DEPARTAMENTO DE ENGENHARIA CIVIL E AMBIENTAL DA FACULDADE DE TECNOLOGIA DA UNIVERSIDADE DE BRASÍLIA COMO PARTE DOS REQUISÍTOS NECESSÁRIOS PARA A OBTENÇÃO DO GRAU DE MESTRE EM ESTRUTURAS E CONSTRUÇÃO CIVIL.

APROVADO POR:

_____

Prof. Francisco Evangelista Junior, PhD. (ENC/UnB)
(Orientador)

_____

Prof. Luiz Guilherme Rodrigues de Mello, PhD. (ENC/UnB)
(Examinador Interno)

_____

Prof. Guilherme Oliveira Ferraz de Paiva, DSc. (IFPI)
(Examinador Externo)

BRASÍLIA/DF, 18 DE DEZEMBRO DE 2024.

FICHA CATALOGRÁFICA

SANTOS, ERICK DOUGLAS DE LUNA
Prediction of stresses in rigid airport pavements considering slab's temperature differential using finite element and machine learning techniques / Erick Douglas de Luna Santos; Orientador: Francisco Evangelista Junior. – Brasília, 2024.

xxiv, 87p., 210 x 297 mm (ENC/FT/UnB, Mestre, Estruturas e Construção Civil, 2024). Dissertação de Mestrado – Universidade de Brasília. Faculdade de Tecnologia. Departamento de Engenharia Civil e Ambiental.

1. Concrete pavements	2. Airports
3. Temperature	4. Machine learning
I. ENC/FT/UnB	II. Título (Mestre)

REFERÊNCIA BIBLIOGRÁFICA

SANTOS, E. D. L. (2024). Prediction of stresses in rigid airport pavements considering slab's temperature differential using finite element and machine learning techniques. Dissertação de Mestrado em Estruturas e Construção Civil. Publicação DM-20A/24, Departamento de Engenharia Civil e Ambiental, Universidade de Brasília, Brasília, DF, 87 p.

CESSÃO DE DIREITOS

AUTOR: Erick Douglas de Luna Santos

TÍTULO: Prediction of stresses in rigid airport pavements considering slab's temperature differential using finite element and machine learning techniques

GRAU: Mestre ANO: 2024

Erick Douglas de Luna Santos
AE 4 Conjunto I/J Torre 1 Apt. 704 – Guará II
71.070-904 Brasília - DF- Brasil
e-mail: erick_ddls@hotmail.com

I dedicate this work to God, my family and friends for all their support and patience during the master's degree.

ACKNOWLEDGMENTS

Firstly, to God for the gift of life and the opportunity to study at the University of Brasilia and participate in the Postgraduate Program in Structures and Civil Construction (PECC). I recognize that without His grace and love none of this would be possible.

I would like to thank my family for all their support, patience and encouragement during my master's degree.

I thank my girlfriend Isadora Rodrigues for having renounced me on many occasions so that I could dedicate myself to the responsibilities of my studies.

I thank my friends who believed and encouraged me during the academic period.

I would like to thank my advisor Francisco Evangelista Junior for all his patience, supervision and guidance during the preparation of the articles and the thesis.

I would like to thank the members of my committee, professors Luiz Guilherme and Guilherme Oliveira, for their availability, notes and evaluation of my work.

ABSTRACT

PREDICTION OF STRESSES IN RIGID AIRPORT PAVEMENTS CONSIDERING SLAB'S TEMPERATURE DIFFERENTIAL USING FINITE ELEMENT AND MACHINE LEARNING TECHNIQUES

Author: Erick Douglas de Luna Santos
Advisor: Francisco Evangelista Júnior
Postgraduate Program in Structures and Civil Construction
Brasilia, December of 2024.

This work aims to develop a machine learning model (ML/RF) to predict maximum tensile stresses in concrete slabs on airport pavements, considering aircraft loads and the linear and nonlinear temperature profile between top and bottom of the concrete slab. From the tensile stress data obtained by finite element simulations, using software ILLISLAB, with A380 and B747 aircraft landing gears and several positive and negative temperature differentials, a dataset was assembled and divided to train and validate the proposed machine learning model. The ML/RF used was Random Forest, through the Scikit-learn Python Library, which provided accurate predictions for different plate thicknesses, tire pressures, load transfer efficiencies between plates, moduli of subgrade reaction, radii of relative stiffness and longitudinal passage positions of the aircraft on the slab path under temperature differential of the concrete slab. The Mean Squared Error obtained by the Random Forest model was equal to 3.60e-4 MPa^2, a maximum absolute error smaller than 0.25 MPa and the majority of the absolute error nearby 0 MPa, all of theses results to the test dataset, showing the reliability of the proposed model.

Keywords: concrete pavements, airports, temperature, machine learning.

RESUMO

PREVISÃO DE TENSÕES EM PAVIMENTOS RÍGIDOS AEROPORTUÁRIOS CONSIDERANDO O DIFERENCIAL DE TEMPERATURA DA PLACA UTILIZANDO ELEMENTOS FINITOS E TÉCNICAS DE MACHINE LEARNING

Autor: Erick Douglas de Luna Santos
Orientador: Francisco Evangelista Júnior, PhD (UnB)
Programa de Pós-graduação em Estruturas e Construção Civil
Brasília, dezembro de 2024.

Este trabalho tem como objetivo desenvolver um modelo de aprendizado de máquina (ML/RF) para predição das tensões máximas de tração em placas de concreto de pavimentos aeroportuários levando em consideração os carregamentos das aeronaves e o perfil de temperatura linear e não linear na espessura da placa. A partir dos dados de tensões obtidos pela modelagem de elementos finitos, utilizando o software ILLISLAB, com trens tipo da aeronave A380 e B747 e diversos diferenciais térmicos na espessura da placa de concreto, foi construído um conjunto de dados utilizado no treinamento e validação do algoritmo. O ML/RF utilizado foi o *Random Forest*, por meio da biblioteca *Scikit-learn* do *Python*, que forneceu predições acuradas para diferentes espessuras, pressões dos pneus, eficiências de transferência de carga entre placas, módulos de reação do subleito, raios de rigidez relativa e posições de passagem longitudinal da aeronave na placa sob diversos diferenciais de temperatura entre o topo e o fundo da placa de concreto. A Média dos Erros Quadrados obtida pelo modelo de Random Forest foi igual a 3.60e-4 MPa^2, um erro absoluto máximo menor do que 0.25 MPa e a maioria dos erros absolutos próximos de 0 MPa, todos os resultados para a base de dados de treinamento, mostrando a confiabilidade do modelo proposto.

Palavras-chave: pavimentos de concreto, aeroportos, temperatura, aprendizado de máquina.

LIST OF FIGURES

LIST OF TABLES

LIST OF ABBREVIATIONS

CG – Center of Gravity

DT – Decision Tree

FAA – Federal Aviation Administration

FEM – Finite Element Method

LTE – Load Transfer Efficiency

MAE – Mean Absolute Error

ML – Machine Learning

ML/RF – Machine Learning Random Forest Model

MSE – Mean Square Error

NAPTF – National Airport Pavement Test Facility

OV – Ordered Values

R^2 - Coefficient of determination

RF – Random Forest

RMSE – Root Mean Square Error

TPC – Complete Landing Gear

TQ – Theoretical Quantity

LIST OF SYMBOLS

Latin Letters

A – Regression coefficient based on the temperature profile measured on the slab

ACL – Passing line

B – Regression coefficient based on the temperature profile measured on the slab

c – Number of different values of a variable

C – Regression coefficient based on the temperature profile measured on the slab

$\hat{c}_b(\boldsymbol{x})$ – Classifier generated from a training set with different weights for its elements

$\hat{c}_{boost}(\boldsymbol{x})$ – Classifier created using boosting technique

D – Number of predictors

$\{D\}$ – Resultant nodal displacements for the whole system

$\{D\}_b$ – Displacement vector of the bar element

$\{D\}_e$ – Displacement vector of the slab element

$\{D\}_s$ – Displacement vector of the spring element

E – Modulus of elasticity of the concrete

$Entropy(X_{i_x})$ – Entropy of a value of an input variable of an input dataset of a decision tree algorithm

$Entropy(Y)$ – Entropy of the output variable of a decision tree algorithm

$\hat{f}_b(\boldsymbol{x})$ – Predictor generated from a training set or bootstrap replica

$\hat{f}_{bag}(\boldsymbol{x})$ – Predictor created using bagging technique

h – Thickness of the concrete slab

IQR – Range between quartiles

k – Modulus of subgrade reaction

$[K]$ – The overall structural stiffness matrix

$\left[K_{Agg}\right]_s$ – Stiffness matrix of the spring element

$\left[K_{top}\right]_e$ – Stiffness matrix of the top layer

$[K_{bot}]_e$ – Stiffness matrix of the bottom layer

$[K_{dowel}]_b$ – Stiffness matrix of the dowel bar

$[K_{sub}]_e$ – Stiffness matrix of the subgrade

l – Tire length and width

L – Free length or width of the slab

ℓ – Radius of relative stiffness

M – Moment

n – Number of data points

$NOLA$ – Nonlinear area

$NOLA_{Q05}$ – The 5th percentile of nonlinear area

p – Number of predictor variables of a training dataset

p_i – Ratio of the number of times a value appears divided by the total number of values of a variable

P – Tire load

P_W – A vertical force

P_{θ_X} – Couple about the X-axis

P_{θ_Y} – Couple about de Y-axis

$\{P\}$ – Equivalent nodal forces for a uniformly distributed load over a rectangular section of the concrete slab

$\{P\}_b$ – Force vector of the bar element

$\{P\}_e$ – Force vector of the slab element

$\{P\}_s$ – Force vector of the spring element

$Q05$ – 5th percentile

$Q25$ – 25th percentile

$Q75$ – 75th percentile

$Q95$ – 95th percentile

T – Temperature

$T(z)$ – Total temperature profile as a function of depth

T_A – Axial temperature component

TB – Stress position in the slab

T_{bot} – Temperature measured at the bottom of the slab

$T_L(z)$ – Linear temperature component as a function of depth

$T_{linear}(z)$ – Linear temperature profile on the concrete slab

T_{mid} – Temperature measured at the middle of the slab

$T_{SES}(z)$ – Non-linear (self-equilibrating) temperature component as a function of depth

T_{top} – Temperature measured at the top of the slab

$Values(X_i)$ = set of different values of an input variable of an input dataset of a decision tree algorithm

W – A vertical deflection in Z-direction

x – Value of an input variable of a Decision Tree algorithm

X_i – Variable of an input dataset of a Decision Tree algorithm

X_{i_x} – Value of a variable of an input dataset of a Decision Tree algorithm

$\left|X_{i_x}\right|$ – Number of times a value appears in a variable of an input dataset of a Decision Tree algorithm

y – Output value of a Decision Tree algorithm

Y – Output variable of a decision tree algorithm

$|Y|$ – Number of values in an output variable of a decision tree algorithm

z – The vertical coordinate measured from the bottom of the slab

Greek Letters

α – Coefficient of thermal expansion of the concrete

β – Bradbury coefficient

β_i – Bradbury coefficient in the direction under investigation

β_j – Bradbury coefficient in the perpendicular direction under investigation

γ – Specific weight of the concrete slab

δ_u – Deflection of the slab without loading

δ_l – Deflection of the slab with loading

ΔT – Linear temperature difference from top to bottom of slab

ΔT_{Q05} – The 5th percentile of linear temperature difference from top to bottom of slab

ΔT_{Q95} – The 95th percentile of linear temperature difference from top to bottom of slab

ε_{ab} – Absolute residual

ε_{ab}^{L} – Absolute residuals for linear stresses predicted by the proposed ML/RF

ε_{ab}^{T} – Absolute residuals for total stresses predicted by the propose ML/RF

θ_X – Rotation about the X-axis

θ_Y – Rotation about the Y-axis

λ – Bradbury parameter

ν – Poisson's ratio of concrete.

ξ – Aircraft type

ρ – Tire pressure

σ – Stress

$\sigma_{\Delta T}$ – Maximum tensile stress predicted by ILLISLAB

$\hat{\sigma}_{\Delta T}$ – Maximum tensile stress predicted by the proposed ML/RF

$\bar{\sigma}_{\Delta T}$ – Average of $\sigma_{\Delta T_i}$ values

$\sigma_{\Delta T=0}$ – Linear stress predicted by the proposed ML/RF to ΔT = 0

σ_A – Axial stress

σ_L – Tensile stress inside the concrete slab with linear distribution

$\sigma_{\Delta T}^{L}$ – Linear tensile stress inside the concrete slab predicted by ILLISLAB

$\hat{\sigma}_{\Delta T}^{L}$ – Linear tensile stress inside the concrete slab predicted by the proposed ML/RF

σ_{SES} – Self-equilibrating stress inside the concrete slab

σ_T – Total stress inside the concrete slab

$\sigma_{\Delta T}^{T}$ – Total tensile stress inside the concrete slab predicted by ILLISLAB

$\hat{\sigma}_{\Delta T}^{T}$ – Total tensile stress inside the concrete slab predicted by the proposed ML/RF

σ_{max} – Maximum total stress

σ_{mean} – Average of total stresses

σ_{min} – Minimum total stress

σ_{Q95} – The 95th percentile of total stress

$\varphi(b)$ – Weight given to the classifier $\hat{c}_b(\boldsymbol{x})$

CONTENTS

1. INTRODUCTION

Rigid airport pavements are commonly used in airport infrastructure, especially on runways and aircraft taxing areas. The design of airport pavements is based on the imposition of aircraft landing gear loads on concrete slabs, mostly considering static loading. Rigid pavement structural analysis has traditionally been based on the maximum flexural stress in the bottom fiber of the slab proposed by Westergaard (1926). His proposal was based on equations that employed simplified assumptions of geometry, loads, and material properties. Over time, several computer programs implemented finite element analyzes trying to make Westergaard's hypotheses more flexible (Huang, 1974; Tia *et al*., 1987; Korovesis, 1990; Khazanovich, 1994; FAA, 2016). With the popularization of the Finite Element Method (FEM) as a computational tool, programs were developed for the analysis of concrete pavements such as ILLISLAB (Tabatabaie, 1980; Koroveses, 1990; Khazanovich, 1994), KENSLAB (Huang, 1973), EverFE (Davids *et al*., 1998) to name a few. The Federal Aviation Administration (FAA) has developed a new airport pavement thickness design procedure called FAARFIELD that incorporates three-dimensional finite element analysis for rigid pavements that calculates the design stress of a concrete slab loaded with trains of standard aircraft types (FAA, 2009a). Additionally, the rigid pavement failure model, which relates the stress estimated by the finite element program to the expected pavement life, has been completely updated based on full-scale tests performed at the National Airport Pavement Test Facility (NAPTF) in 2004 (FAA, 2009b; FAA, 1997a; FAA, 1997b).

The concrete slab exhibits a phenomenon called thermal warping related to climatic conditions depending on the time of day and the seasons. Thermal warping causes compression and tensile stresses in the slab, causing curvature in the pavement, discomfort to the user, and changing in stress distribution (Huang, 2003; Balbo, 2009). Experimental and analytical studies have reported the influence of temperature differential on concrete pavement analysis (Huang, 2003; Khazanovich, 1994). Therefore, the critical stresses in these pavements result in combinations of the temperature induced stresses on top and bottom of the concrete slab and superimposed traffic loads. As the slab warps, the simple superposition of mechanical loads and environmental temperature often does not correspond to their simultaneous effect and responses (Khazanovich and Ioannides 1994; Thompson and Barenberg 1992). Especially in realistic conditions, in which the loss of contact between the

concrete slab and the foundation, due to the thermal warping, generates a distribution that induces non-linearity of responses, making the superposition between mechanical and environmental loads (thermal differentials) inadequate. This complexity demands the development and use of sophisticated finite element modeling in order to account this nonlinear effect during slab warping.

Investigations into the effect of temperature distribution on pavements have been carried out over the years, particularly for rigid road pavements with Severi (2002), Balbo and Severi (2002), Hiller and Roesler (2002) Rufino and Roesler (2005), Fonteles (2017) among the most comprehensive ones. Severi (2002) and Balbo and Severi (2002) monitored the temperature of 15 instrumented concrete pavement slabs in São Paulo, Brazil, for more than a year, and analyzed the influence of climatic conditions such as daily temperature and humidity and seasonal variations of temperature differentials across plate depth with temperature differentials above 15 °C observed. Non-linear temperature distributions along the thickness of the plates were also monitored. Hiller and Roesler (2002) used finite element analysis to compare critical tensile stresses for typical concrete pavements in California, United States. A parametric study was conducted investigating the influence of wheel passage, subgrade reaction modulus, concrete slab geometry, temperature differential and type of road axis. Rufino and Roesler (2005) also analyzed the effect of temperature curling on the measured strain and deflection responses for a several aircraft and load locations. More recently, Fonteles (2017) developed a computational model composed of 16 concrete plates and analyzed the acting stresses using the ILLISLAB finite element program. The stresses were analyzed considering the linear and non-linear thermal differential and their effect on the stresses at the bottom and top of the plate, based on the temperatures of São Paulo, Brazil, and Sacramento, United States, using the work of Severi (2002) and Hiller and Roesler (2002), respectively. Despite being efficient, finite element models still require relevant computational modeling costs, especially when using specialized models for stress prediction considering more realistic hypotheses of mechanical loading coupled with temperature distribution and loss of contact between the concrete slab and its foundation.

Recent literature presents some work using Machine Learning (ML) techniques to predict several variables in rigid pavements, such as the surface roughness index of the concrete slab (Suliman *et al*., 2024); transverse cracks (Pasupunuri, Thom and Li, 2023); surface pathologies (Jung *et al*., 2024); bending stresses inside the concrete slabs from stress

and temperature data measured on 4 taxiways at John F. Kennedy International Airport (Gungor and Al-Qadi, 2018). The literature does not present any work that uses machine learning techniques for prediction, and consequent replacement of finite element models.

Based on the above context, this thesis aims to develop a Random Forest (RF) machine learning model for predicting maximum tensile stresses in concrete slabs of airport pavements considering the loads of A380 and B747 aircraft and the temperature profile in the slab thickness. From the stress data obtained by finite element modeling, the prediction model was built considering different plate thicknesses, tire pressures, load transfer efficiencies between the plates, subgrade reaction moduli, relative stiffness radii and positions of longitudinal passage of the aircraft on the plate under various temperature differentials between the top and bottom of the concrete plate. The results show that the achieved model achieved good accuracy in predicting tensile stresses, making it capable of replacing finite element modeling with the conditions of the variables considered.

1.1. OBJECTIVES

1.1.1. General Objectives

This work has the general objective of predicting maximum linear, self-equilibrating and total stresses in rigid airport pavements, considering the temperature profile and design variables involved, through the application of Machine learning techniques developed from a database of data formed with results generated by scientific productions.

1.1.2. Specific Objectives

- Extract and analyze tensile stresses and temperatures data on concrete pavements produced by scientific work;
- Apply Random Forest (ML/RF) to predict linear, self-balancing and total stresses generated as a function of the temperatures profile;
- Apply Random Forest model and verify his capacity of generating satisfactory outputs substituting the use of finite element method;
- Verify the capacity of the ML/RF model to predict stresses on rigid airport pavements in several different conditions and variables, such as aircraft model (A380 or B747), tire pressure, degree of non-linearity, temperature, among other variables.

1.2. THESIS ORGANIZATION

This thesis was structured into five chapters including this one: introduction (the first), theoretical background (the second), methodology (the third), results and discussions (chapter four), and conclusion (chapter five).

The first chapter contains the contextualization of the problem studied, a general overview of existing solutions, their importance, in addition to showing the objectives to be achieved.

In the second chapter, the theoretical background regarding stresses in concrete slabs, temperature profile and Machine Learning is explained.

In the third chapter, the methodology used to develop the Random Forest is shown, highlighting the steps involved to achieve the proposed objectives.

In the chapter four, the results that validate the RF in its three outputs and the measurements obtained from the analysis of São Paulo's temperature data are discussed.

In chapter five, the conclusion and suggestions for future work are presented.

2. THEORETICAL BACKGROUND

Next, some concepts relevant to understanding the topic will be presented, aiming to clarify aspects that impact the prediction of stresses in rigid airport pavements. To this end, this section was divided into three parts: the first focused on the presentation of important concepts related to stress on rigid pavements, the second focused on the nonlinear temperature profile and the third focused on the algorithm of machine learning used for predictions of maximum stresses.

2.1. PREDICTION OF STRESSES ON RIGID PAVEMENT

Thermal warping is caused by the incidence of heat and radiation from the sun on the surface of concrete slabs. This phenomenon occurs because concrete is not a good conductor of heat, so there is a thermal differential throughout its thickness, generating a curvature in the pavement that varies along the day (Huang, 2003). During the day, the temperature at the top of the slab is higher than at the bottom, generating a downward curvature. And during the night, the process reverses, the temperature at the bottom of the slab is higher than at the top, generating an upward curvature as can be seen in Figure 2.1.

Figure 2.1 - Curvature of concrete slabs depending on temperature difference: a) Night ($T_{top} < T_{bot}$); b) Day ($T_{top} > T_{bot}$)

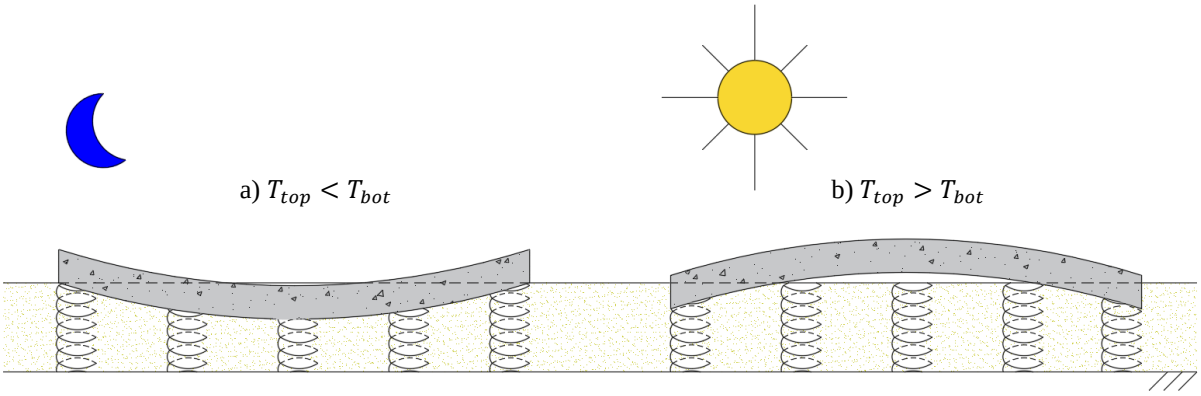

Source: Author.

One of the main foundation models used to model the behavior of rigid pavements is the Winkler foundation, also known as dense liquid foundation. This type constitutes a classic model used for slabs on the ground that can be represented by a set of imaginary individual springs. These springs are characterized by a stiffness parameter *k*, called the modulus of subgrade reaction, which represents the elasticity of the subgrade soil, and it is assumed that they act independently of each other and deform due to the loads arising from the self-weight of the concrete plate as can be seen in Figure 2.1.

The pioneering equations for predicting stresses due to thermal differentials were developed by Westergaard (1927) to characterize the tensile stress inside the concrete slab with linear distribution (σ_L) and infinite size (Equation (2.1)):

$$\sigma_L = \frac{E\alpha\Delta T}{2(1-\nu)} \tag{2.1}$$

where E = modulus of elasticity of the concrete (MPa); α = coefficient of thermal expansion of the concrete (1/°C); ΔT = linear temperature difference from top to bottom of slab (°C); and ν = Poisson's ratio of concrete.

However, Bradbury (1938) improved the Equation (2.1) by adding a parameter that corrects the formulation for a slab of finite size, according to the Equation (2.2):

$$\sigma_L = \frac{E\alpha\Delta T}{2(1-\nu)}\left(\beta_i + \nu\beta_j\right) \tag{2.2}$$

where β_i = Bradbury coefficient in the direction under investigation; and β_j = Bradbury coefficient in the perpendicular direction under investigation.

where β can be written as Equation (2.3):

$$\beta = 1 - \frac{2\cos(\lambda)\cosh(\lambda)\,(\tan(\lambda) + \tanh\,(\lambda))}{sen(2\lambda) + senh(2\lambda)} \tag{2.3}$$

where λ is defined by the Equation (2.4):

$$\lambda = \frac{L}{\ell\sqrt{8}} \tag{2.4}$$

where L = free length or width of the slab; and ℓ radius of relative stiffness.

The radius of relative stiffness is then defined by Equation (2.5):

$$\ell = \sqrt[4]{\frac{Eh^3}{12(1-\nu^2)k}} \tag{2.5}$$

where h = depth of the concrete slab; and k = modulus of subgrade reaction.

One of the ways to determine the transfer of loads between slabs is defined through the deflections generated in neighboring slabs through a load applied to the edge of one of them, Load Transfer Efficiency (LTE), and is expressed through the Equation (2.6) and can be better understood through the Figure 2.2, showing the parameters used and the representation in the Finite Element Method:

$$LTE = \frac{\delta_u}{\delta_l}100\% \tag{2.6}$$

where δ_u = deflection of the slab without loading; and δ_l = deflection of the slab with loading.

Figure 2.2– a) Demonstration of parameters used to calculate LTE; b) Representation of rigid transversal element that simulate LTE in Finite Element Method

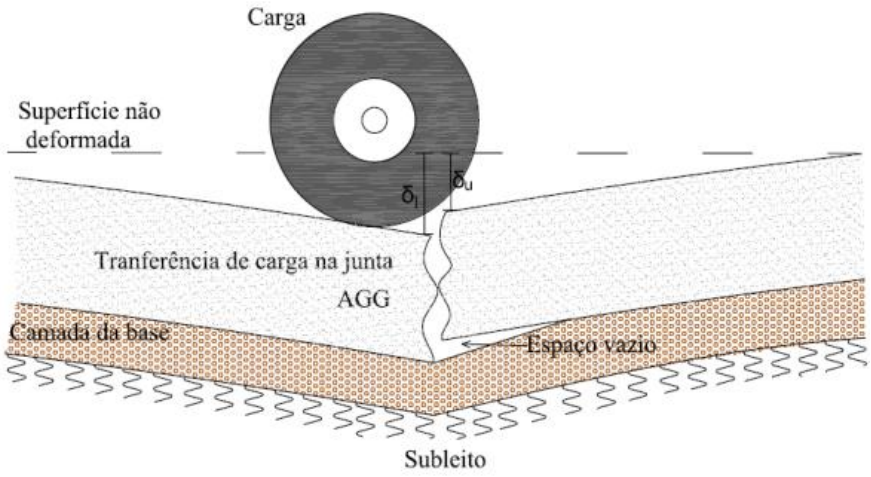

a)

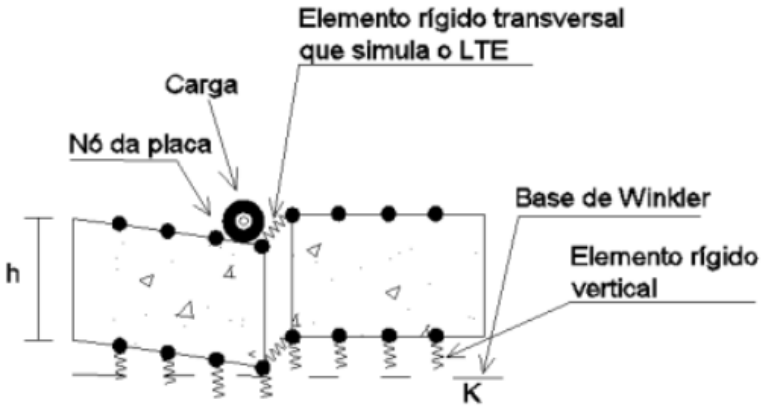

b)

Source: Fonteles (2017)

2.2. NONLINEAR TEMPERATURE PROFILE

Thomlinson (1940) divided the total temperature profile as a function of depth ($T(z)$) into three parts: axial temperature component (T_A) that causes axial displacement (expansion or contraction), linear temperature component as a function of depth ($T_L(z)$) that causes the bending and non-linear (self-equilibrating) temperature component as a function of depth ($T_{SES}(z)$) as shown in Figure 2.3 and Equation (2.7), with the total stress being the resultant generated from the sum of these three components:

Figure 2.3 – Components of the total temperature profile

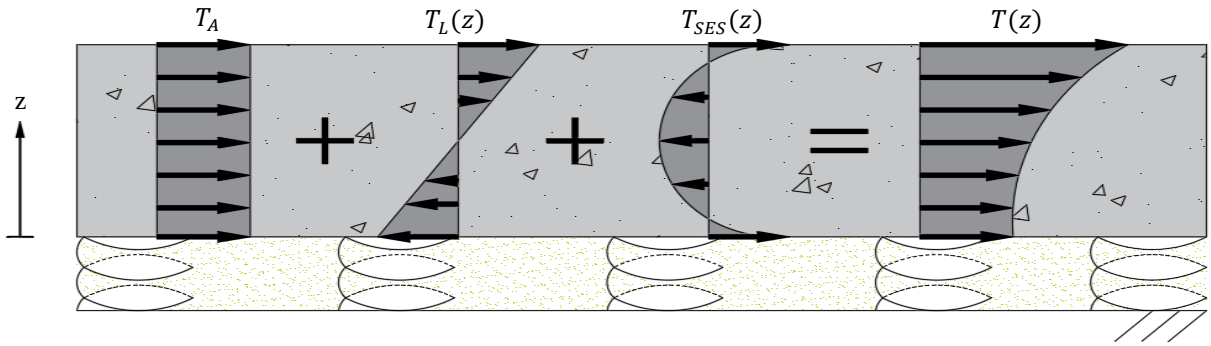

Source: Author.

$$T(z) = T_A + T_L(z) + T_{SES}(z) \tag{2.7}$$

In which T_A is generated from a uniform change in temperature, it causes an expansion or retraction of the plate and generates a constant stress when it comes into contact with another and due to contact with underlying layers, however, the stress generated is usually treated as negligible because this restraint in generally assumed to be minimal or unrestrained, due to the loss and subsequent partial recovery of full contact between the slab and the subgrade, and therefore this axial strain would not result in significant slab stresses and is generally ignored, however, at early concrete ages this assumption is not valid (Hiller and Roesler, 2002; Hiller, 2007; Ioannides and Khazanovich, 1998), $T_L(z)$ is the equivalent linear bending strain derived from the nonlinear temperature profile assuming either of the following two conditions: the plate must be fully restrained or have a significant self-weight (Hiller, 2007) and $T_{SES}(z)$ is the non-linear self-equilibrating internal strains such that all forces and bending moments due to this component of the non-linear temperature profile are self-balancing (Hiller, 2007), it affects the compressive and tensile strains in the slab at different depths, however does not affect the deflection profile (Ioannides and Khazanovich, 1998). The division of the temperature profile into these three components is based on the assumption used in classical plate-bending theory that the cross section of a plate remains plane after bending (Choubane and Tia, 1992).

Choubane and Tia (1992) performed a comparative study of existing models for real temperature distributions and an analysis of temperature data and demonstrated that a quadratic polynomial can be used to represent the distribution across the depth of the slab. This polynomial function can be represented by the Equation (2.8):

$$T(z) = A + Bz + Cz^2 \tag{2.8}$$

where A, B and C are regression coefficients based on the temperature profile measured on the slab and z is the vertical coordinate measured from the bottom of the slab described according to the Equations (2.9), (2.10) and (2.11).

$$A = T_{bot} \tag{2.9}$$

$$B = \frac{4T_{mid} - 3T_{bot} - T_{top}}{h} \tag{2.10}$$

$$C = \frac{2\left(T_{bot} + T_{top} - 2T_{mid}\right)}{h^2} \tag{2.11}$$

where T_{top} = temperature measured at the top of the slab ($z = h$), T_{mid} is the temperature measured in the middle of the slab ($z = h/2$), T_{bot} is the temperature measured at the bottom of the slab ($z = 0$) and h is the thickness of the slab.

The temperature component causing axial displacement is determined by integrating the temperature across the section and dividing the integral by the slab thickness, as can be seen in the Equation (2.12).

$$T_A = \frac{1}{h}\int_0^h (A + Bz + Cz^2)dz = A + B(h/2) + C(h^2/3) \tag{2.12}$$

The temperature component causing bending of the slab is determined by taking the moment of the area that remains after the axial component is subtracted from the total area under the curve and the finding a linear temperature distribution that would produce the same moment. The moment is taken with respect to the mid-depth of the slab. Let $z' = (h/2) - z$. Then we arrive at the Equation (2.13):

$$\begin{aligned} T(z) - T_A &= Bz + Cz^2 - B(h/2) - C(h^2/3) \\ &= -C(h^2/12) - (B + Ch)z' + Cz'^2 \end{aligned} \tag{2.13}$$

The moment, taken with respect to slab mid-depth, will be according to the Equation (2.14).

$$M = \int_{-h/2}^{h/2} (T(z) - T_A)z'dz' = -(B + Ch)h^3/12) \tag{2.14}$$

For linear temperature distribution varying from $+T_L$ to $-T_L$, the moment caused by this temperature is described by the Equation (2.15).

$$M = 2T_L(h/4)(h/3) = T_L(h^2/6) \tag{2.15}$$

By setting this moment equal to the moment as expressed in Equation (2.14), $T_L(z)$ at any depth z can be solved to be according to the Equation (2.16).

$$T_L(z) = (B + Ch)[z - (h/2)] \tag{2.16}$$

Last, the nonlinear temperature component is determined by the Equation (2.17).

$$\begin{aligned} T_{SES}(z) &= T(z) - T_A - T_L(z) \\ &= C[z^2 - hz + (h^2/6)] \end{aligned} \tag{2.17}$$

Several authors, such as Choubane and Tia (1995), Mohamed and Hansen (1997), Ioannides and Khazanovich (1998) and Rodden (2006) have developed and presented the formulation to calculate the total curling stress based on axial, linear and non-linear components. Taking as a basis the formulation developed by the authors, we can arrive at the formulation of the self-equilibrating stress (σ_{SES}) (Equation (2.18)).

$$\sigma_{SES} = C\,\frac{E\alpha}{1-\nu}\left[z^2 - hz + \frac{h^2}{6}\right] \tag{2.18}$$

Bearing in mind that nonlinear temperature profiles can have an impact on the emergence of stresses and fatigue of the structure, Hiller and Roesler (2010) developed a parameter called nonlinear area (NOLA), which is defined by the area between the real temperature profile $\left(T(z)\right)$ and the linear temperature profile $\left(T_{linear}(z)\right)$ on the slab, which is described by the Equation (2.19).

$$T_{linear}(z) = \frac{\left(T_{top} + T_{bot}\right)z}{h} \tag{2.19}$$

This parameter reveals the level of nonlinearity in any distribution, which can be related to the self-equilibrating stress (σ_{SES}). And it can be described mathematically by the Equation (2.20):

$$NOLA = \int_0^h [T(z) - T_{linear}(z)]dz \tag{2.20}$$

If we use the Equations (2.9) to (2.11), substitute in (2.8) and apply in (2.20), we obtain the Equation (2.21):

$$\begin{aligned} NOLA = \int_0^h \Bigg[& T_{bot} + \frac{4T_{mid} - 3T_{bot} - T_{top}}{h}z \\ & + \frac{2\left(T_{top} + T_{bot} - 2T_{mid}\right)}{h^2}z^2 - \frac{\left(T_{top} + T_{bot}\right)}{h}z\Bigg]dz \end{aligned} \tag{2.21}$$

When solving the integration, Equation (2.22) is obtained:

$$NOLA = \frac{2T_{mid} - T_{bot} - T_{top}}{3}h \tag{2.22}$$

When we isolate T_{mid} in Equation (2.22) and substitute in (2.11), we arrive at Equation (2.23):

$$C = \frac{-6NOLA}{h^3} \tag{2.23}$$

Substituting (2.23) into (2.18), we arrive at Equation (2.24):

$$\sigma_{SES} = \frac{-6NOLA}{h^3}\frac{E\alpha}{1-\nu}\left[z^2 - hz + \frac{h^2}{6}\right] \tag{2.24}$$

Finally, when we apply the Equation (2.24) to $z = h$ and $z = 0$ we arrive at Equation (2.25), which describes the stresses at the top and bottom of the slab:

$$\sigma_{SES}(h) = \sigma_{SES}(0) = \frac{-NOLA}{h}\frac{E\alpha}{1-\nu} \tag{2.25}$$

Or, substituting the Equation (2.22), we arrive at Equation (2.26).

$$\sigma_{SES}(h) = \sigma_{SES}(0) = \frac{(T_{top} + T_{bot} - 2T_{mid})}{3}\frac{E\alpha}{1-\nu} \tag{2.26}$$

2.3. MACHINE LEARNING MODELS (DECISION TREE AND RANDOM FOREST)

To better understand Random Forest, it is necessary to know more about Decision Tree (DT). DT is a Machine Learning technique that builds a hierarchical decision structure based on the analysis of variables (Mueller, Kusne and Ramprasad, 2016). As can be seen in Figure 2.4, with x being the input value, which goes through several decision points until reaching the result (y), output value.

Figure 2.4 - Structure of the algorithm with decision trees: a) Decision Tree (DT); b) Random Forest (RF)

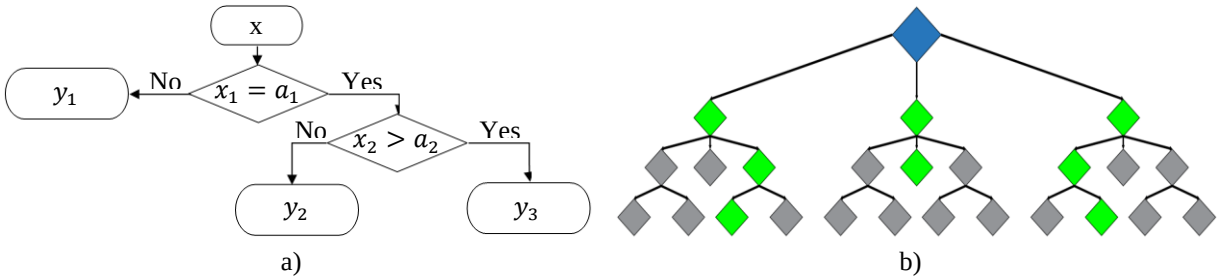

Source: Author.

The algorithm has a criterion for the choice of the position of each decision point (or also known as node) that is made based on the Equation (2.27) that calculate the entropy (or

disorganization) of the output variable (Y) of the database of training and the Equation (2.28) that calculate the information gain of each variable of an input dataset (X_i).

$$Entropy(Y) = \sum_{i=1}^{c} -p_i \log_2 p_i \tag{2.27}$$

where c = the number of different values of the output variable; and p_i = the ratio of the number of times a value appears divided by the total number of values of the output variable.

$$Gain(Y, X_i) = Entropy(Y) - \sum_{x \in Values(X_i)} \frac{|X_{i_x}|}{|Y|} Entropy(X_{i_x}) \tag{2.28}$$

where $|Y|$ = number of values in the output variable; $|X_{i_x}|$ = number of times a value appears in an input variable; $Entropy(X_{i_x})$ = entropy of a value of an input variable; $Values(X_i)$ = set of different values of an input variable; and x = value of an input variable.

The variables that present the highest information gain values remain at the top of the hierarchy (also known as the root of the tree). From this, branches arise according to the number of different values of the root variable and the process restarts for each existing branch, excluding the variable that gave rise from the process, repeating this until only existing one variable to be analyzed in each branch and generating the output values, these being the leaves of the tree (Mueller, Kusne and Ramprasad, 2016). However, depending on how the data set is subdivided between training and testing, DTs can produce different responses, that is, they have a large variance. Therefore, the following techniques aim to reduce this variance.

Also known as bootstrap aggregating, this technique aims to create several versions of a predictor from different training sets ($\hat{f}_b(\boldsymbol{x})$) and build a predictor based on the combination of these versions ($\hat{f}_{bag}(\boldsymbol{x})$), with the variance of this final predictor being smaller than that of the predictors that gave rise to it. In other words, a series of weak forecasters (with a high error rate) are considered to obtain a strong forecaster (with a low error rate). However, considering that, in general, there are not several training sets, bootstrap replicas are used (i.e., simple random samples with replacement of the same size as the initial set, with each element having the same probability of being selected) of the training set to obtain the different versions of the predictors (Morettin, 2022). As can be better understood through Equation (2.29).

$$\hat{f}_{bag}(\boldsymbol{x}) = \frac{1}{D}\sum_{b=1}^{D} \hat{f}_b(\boldsymbol{x}) \tag{2.29}$$

where D = the number of predictors; and $\hat{f}_b(\boldsymbol{x})$ = the predictor generated from a training set or bootstrap replica.

Unlike the bagging technique, in boosting the trees are built in sequence from the training set, with each element having a distinct and variable weight (or probability) of being selected, therefore, poorly classified elements in a predictor receive greater weights in the selection of the following tree, therefore, cases in which classification is more difficult receive greater attention. Therefore, the final classifier ($\hat{c}_{boost}(\boldsymbol{x})$) is built through the D weak classifiers generated in sequence from different trees, with the classification of each element applied through the majority vote principle. Furthermore, the classifiers also receive weights depending on their error rates, with the strong classifier being described by Equation (2.30) (Morettin, 2022). Both bagging and boosting have the same purpose, reducing variance and bias, however the second can reduce bias better than the first (the representation of working of both of them can be seen in the Figure 2.5).

$$\hat{c}_{boost}(\boldsymbol{x}) = \sum_{b=1}^{D} \hat{c}_b(\boldsymbol{x})\varphi(b) \tag{2.30}$$

where $\varphi(b)$ = weight given to the classifier $\hat{c}_b(\boldsymbol{x})$; and $\hat{c}_b(\boldsymbol{x})$ = classifier generated from a training set with different weights for its elements.

Figure 2.5 – Representation of algorithms of reduction of bias and variance (Bagging and Boosting)

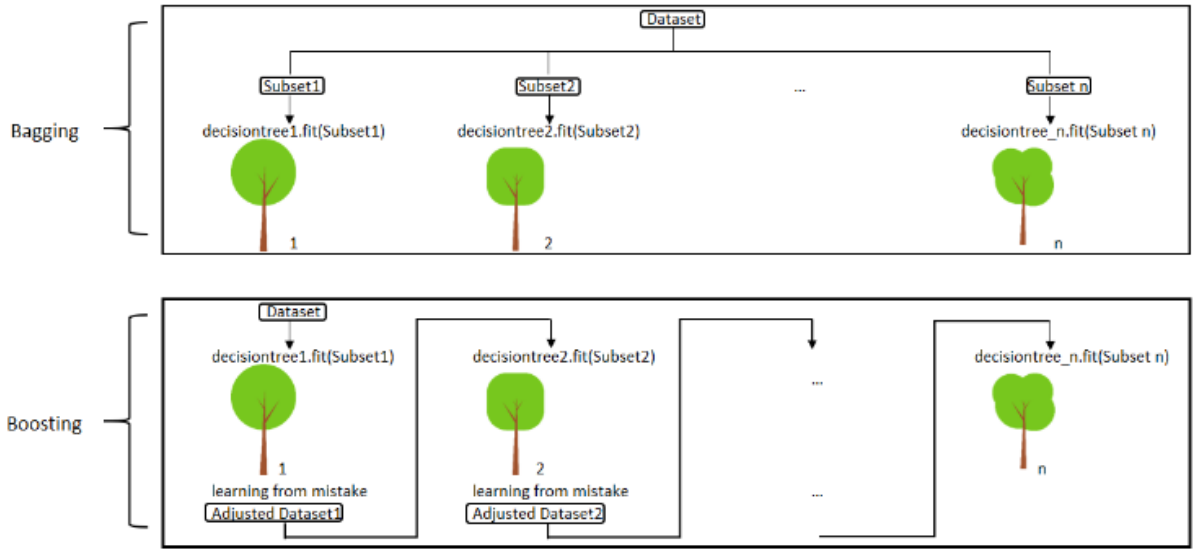

Author: Machine Learning Plus (2024)

Different from the model used by bagging and boosting techniques, in which they use a set of D trees using the same amount p of predictor variables, Random Forest uses different sets of predictor variables in the construction of each tree, that is, in a certain way, it can be said that it applies the bagging technique to the set of p predictor variables, introducing more randomness and diversification in the process of creating the final (aggregated) model (Morettin, 2022).

In general, Random Forest generates fewer variable outputs compared to those obtained through bagging, in which strong predictors are usually selected at the root node, generating very similar trees, not contributing to reducing the variability of predictions. Contrary to this, in random forests, strong predictors do not tend to be selected in the division of all nodes, producing less correlated results and the "average", obtained by the majority vote, generally reduces variability. Furthermore, the accuracy of Random Forest adjustment is equal to or exceeds boosting, in general, it is more robust if we consider outliers and noise, and it is also faster when compared to other techniques (Morettin, 2022).

Decision trees are best suited when the relationship between the predictor variables and responses does not follow a linear model, otherwise, linear regression is recommended. In the case of DT, some predictor variables can be qualitative, and there is no need to transform them into dummy variables, as is done in regression models. The purpose used in this model is similar to those applied in classification models: subdividing the space generated by the explanatory variables into several regions and adopting the average responses of each of them as predictors, with the regions being selected in such a way that they produce the smallest Mean Square Error (MSE) or the lowest coefficients of determination (R^2) (Morettin, 2022).

Kawsar, Serker and Afsana (2024) tested Artificial Neural Network, Support Vector Machine, Decision Tree, Random Forest and Linear Regression to predict the strength of concrete using a database from the University of California containing 1030 samples and Random Forest obtained the best results, being much superior to the others. Suliman *et al.* (2024) applied Linear Regression, Multivariate Adaptive Regression Splines, Gaussian Process Regression and Artificial Neural Network in a database with 1414 data and 21 variables to predict the International Roughness Index of concrete pavement plans, with Deep Artificial Neural Network presented the best results. Pasupunuri, Thom and Li (2023) tested Decision Tree Regression, Random Forest Regression and Deep Neural Network to predict transverse cracks in planes of joined concrete pavements and the latter obtained the best results. Jung *et al*. (2024) developed a Machine Learning model capable of predicting

pathologies on the surface of a concrete pavement. They used Particle Filtering, known for its performance in time series analysis, being compared with Long Short-Term Memory Networks and Deep Neural Networks and proving superior to them. Gungor and Abd Al-Qadi (2018) used Support Vector Machine with the aim of calculating the temperature, curvature and bending stresses inside the pavement using data from 4 taxiways at John F. Kennedy International Airport and obtaining satisfactory results. Different from the previous works, this thesis used Random Forest technique to create a model to predict tensile stresses in concrete airport pavements using data obtained by Finite Element Method through ILLISLAB in order to substitute this method and generated better results creating a model that achieved a R^2 near 100%.

3. METHODOLOGY

To achieve the proposed objective, predicting linear, self-balancing and total stresses in rigid airport pavements, the Equation (3.1) was used, being this equation obtained from the Equation (2.7), as can be seen in the Equation (3.2):

$$\sigma_T(z) = \sigma_L(z) + \sigma_{SES}(z) \tag{3.1}$$

where $\sigma_T(z)$ = total stress, $\sigma_L(z)$ = linear stress; and $\sigma_{SES}(z)$ = self-equilibrating stress, all of them as a function of depth.

$$\left(T(z) = T_A + T_L(z) + T_{SES}(z)\right)\frac{E\alpha}{1-\nu} \rightarrow \sigma_T(z) = \sigma_A + \sigma_L(z) + \sigma_{SES}(z) \tag{3.2}$$

The axial stress (σ_A) is usually treated as negligible, so for the purposes of this study it was not considered, as explained in Section 2.2. Note that it is enough to predict the linear and total stresses to obtain the self-equilibrating. Due to this, it was decided to create two models, one responsible for predicting the linear stresses and the other responsible for predicting the total stresses and the self-equilibrating stresses being obtained from the subtraction of both values. This decision was made aiming to obtain models with better results, less time for processing and less space of storage.

To create the machine learning model (ML/RF), three steps were followed, which consisted of: extracting data from finite element simulations through ILLISLAB software, using software GetData Digitizer, building the dataset, and training and validating the ML/RF technique using Python and its available libraries, according to the Figure 3.1, in which each step will be better described in the Sections 3.1 to 3.3:

Figure 3.1 – Flowchart summary of the methodology

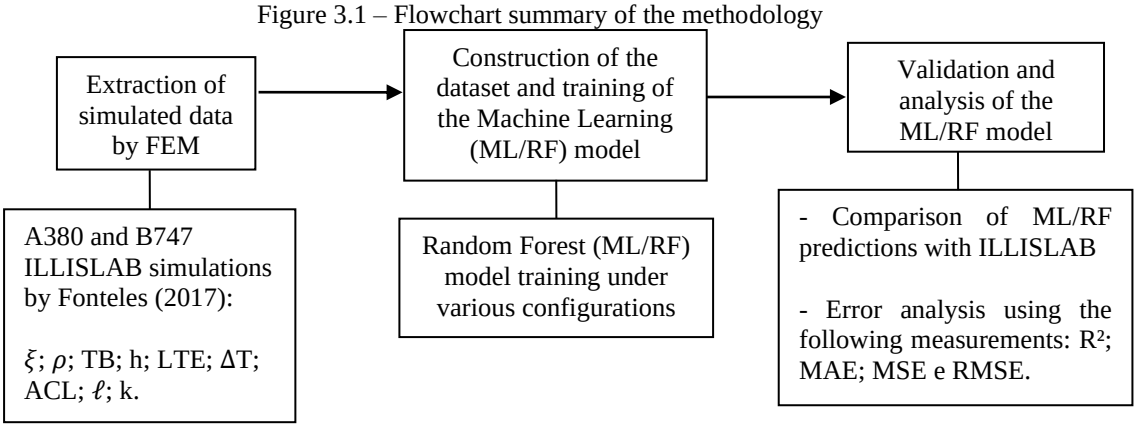

Source: Author.

3.1. FINITE ELEMENT SIMULATIONS DATA

To develop the work, it was necessary to gather stress values obtained by FEM in different scenarios, including different temperature differentials (ΔT) along the slab´s thickness, from airport concrete pavement slabs. To this end, the work of Fonteles (2017) was selected, which presents the data mentioned above, necessary for the research. The data were extracted using the GetData Digitizer software and organized into tables. Fonteles (2017) used the ILLISLAB software, a program developed at the University of Illinois at Urbana – Champaign, which allows numerical simulation by varying linear and non-linear temperature distributions, making it possible to obtain stresses in rigid pavements under different configurations. ILLISLAB makes the analysis in two steps providing a reasonable approach: first, a two-dimensional analysis of the whole concrete pavement and then a three-dimensional analysis of a small section of the joint that uses the results of the two-dimensional analysis in terms of the proper boundary condition (Tabatabaie and Barenberg, 1978). The software uses a concrete pavement slab model developed by Melosh (1963), represented by a rectangular plate element with four nodes (one in each corner) with three displacement components – a vertical deflection (W) in Z-direction, a rotation (θ_X) about the X-axis, and a rotation (θ_Y) about the Y-axis – and corresponding to these displacement components, there are three force components – a vertical force (P_W), a couple about the X-axis (P_{θ_X}), and a couple about the Y-axis (P_{θ_Y}), respectively (Tabatabaie and Barenberg, 1978; Khazanovich, 1994). For each element, these forces and displacement can be related by matrix notation, as can be seen in the Equation (3.3) :

$$\{P\}_e = [K_{top} + K_{bot} + K_{sub}]_e \{D\}_e \quad (3.3)$$

where $[K_{top}]_e$ = the stiffness matrix of the top layer; $[K_{bot}]_e$ = the stiffness matrix of the bottom layer; $[K_{sub}]_e$ = the stiffness matrix of the subgrade; $\{P\}_e$ = the force vector of the slab element; and $\{D\}_e$ = the displacement vector of the slab element.

A bar with two degrees of freedom/node is used to model the dowel bars at the joints. The two displacement components at each node are a vertical displacement (W) in the Z-direction and a rotation (θ_Y) about the Y-axis, and their corresponding force (P_W) and couple about the Y-axis (P_{θ_Y}), respectively (Tabatabaie and Barenberg, 1978; Khazanovich, 1994). The force-displacement relation can be written according to the Equation (3.4).

$$\{P\}_b = [K_{dowel}]_b \{D\}_b \quad (3.4)$$

where $[K_{dowel}]_b$ = the stiffness matrix of the dowel bar; $\{P\}_b$ = the force vector of the bar element; and $\{D\}_b$ = the displacement vector of the bar element.

The relative deformation of the dowel bar and surrounding concrete is represented as the stiffness of a vertical spring element that extends between the dowel bar and the surrounding concrete at the joint face. This displacement component at each node is a vertical displacement (W) in the Z-direction, and the corresponding force component is a vertical force (P_W) (Tabatabaie and Barenberg, 1978; Khazanovich, 1994). The force-displacement relation for a spring element can be written according to the Equation (3.5).

$$\{P\}_s = [K_{Agg}]_s \{D\}_s \quad (3.5)$$

where $[K_{Agg}]_s$ = the stiffness matrix of the spring element; $\{P\}_s$ = the force vector of the spring element; and $\{D\}_s$ = the displacement vector of the spring element.

The overall structural stiffness matrix $[K]$ is formulated by superimposing the effects of the individual element stiffnesses by using the topological (or the element-connecting) properties of the pavement system and used to solve the set of simultaneous equations that have the form according to the Equation (3.6) (Tabatabaie and Barenberg, 1978; Khazanovich, 1994).

$$\{P\} = [K] \{D\} \quad (3.6)$$

where $\{P\}$ = equivalent nodal forces for a uniformly distributed load over a rectangular section of the concrete slab; and $\{D\}$ = resultant nodal displacements for the whole system.

Fonteles (2017) built a model with 16 square slabs measuring 7.62 meters on a side, varying thicknesses of 0.250, 0.406 and 0.508 meters, and LTE of 0 and 85% in both directions, choosing slab 11 as the control one to predict the stresses in all analyzes, as shown

in Figure 3.2 along with the position of all set of slabs and the finite element mesh used by the author.

Figure 3.2 - Model of concrete pavement slabs in FEM developed by Fonteles (2017): a) set of slabs; b) detail of the finite element mesh

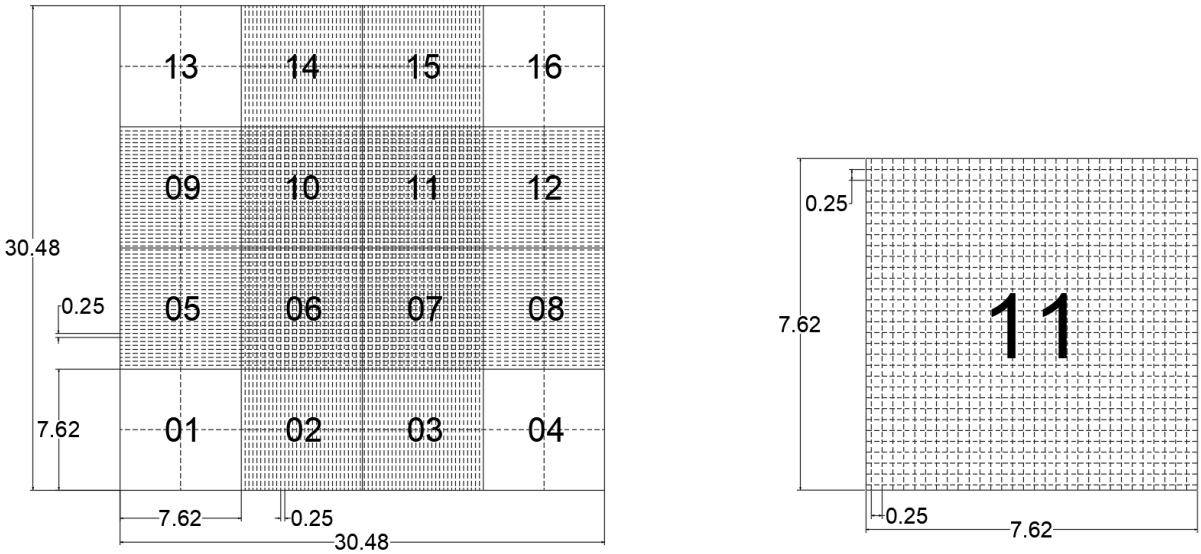

a) b)

Source: Author.

For this thesis, the loading of the A380 and B747 aircraft was used considering the complete landing gear (TPC) as detailed in Figure 3.3. Tire pressure (ρ) equal to 1.38 MPa (200 psi) was used, square tires with 0.38 m (15 inches) of side and 200,349.86 N (45,000 pounds) of load per tire.

Figure 3.3 - Dimensions of the landing gears used by Fonteles (2017) as loading: a) A380 (TPC); b) B747 (TPC). Units in meters

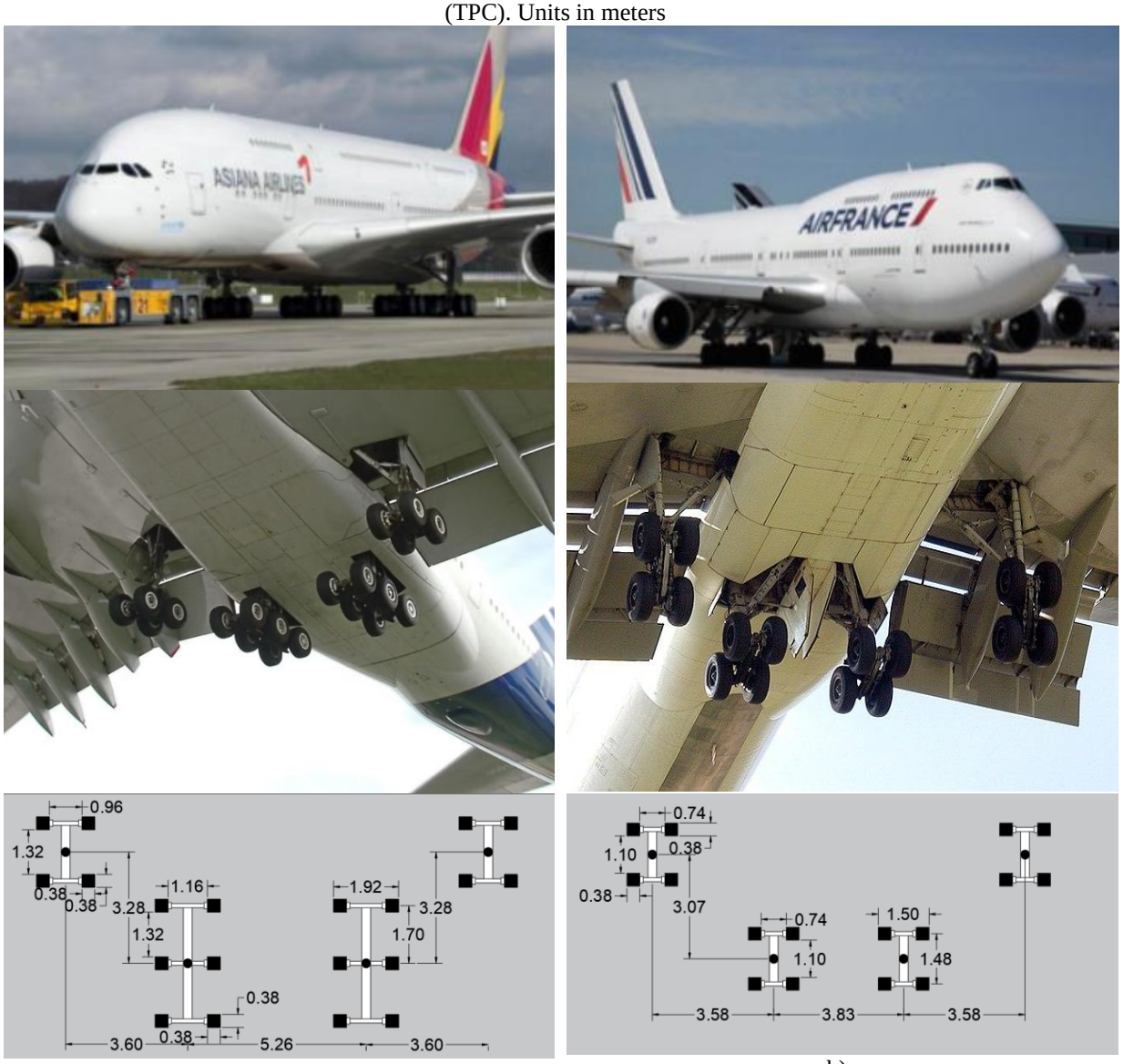

a) b)

Source: Author; Pictures: Air Journal (2016)

Other parameters of pavement geometry, material properties and loads that were assumed constant for training the ML/RF model are listed in Table 3.1.

Table 3.1 - Constant parameters and properties.

Parameter or property	Values
Plate length and width (L) [m]	7.62
Tire length and width (l) [m]	0.38
Modulus of elasticity (E) [MPa]	31,000
Thermal expansion coefficient (α) [1/°C]	5.0e-6
Poisson's ratio (ν)	0.15
Specific weight (γ) [kg/m³]	2,408.15
Tire pressure (ρ) [MPa]	1.38
Tire load (P) [N]	200,349.86

Source: Author.

The aircraft's landing gear arrangement on the slabs was represented by the center of gravity (CG) of the landing gears showed in Figure 3.3, varying 0.25 m along the transverse joint and 0.38 m along the longitudinal joint (as can be seen in the Figure 3.4). Therefore, the passing lines (ACL 1 to 17) were named in a way that ACL1 is the passing line in which the CG is over the longitudinal joint of slab 11, ACL2 has the CG passing 0.25 m off that longitudinal joint towards the interior of slab 11, and so forth (Figure 3.5). All positions along the passing lines from ACL1 to ACL17 were simulated with different temperature differentials (ΔT) to cover a wide range of possible temperature differentials occurring into the slabs. For each application of loading on slab (ACL or LP), Fonteles (2017) gathered the greatest tensile stresses presented at whole slab, for each configuration, creating graphs like Figure 3.6, the sources of data used by this work.

Figure 3.4 - The aircraft's landing gear arrangement on the slabs

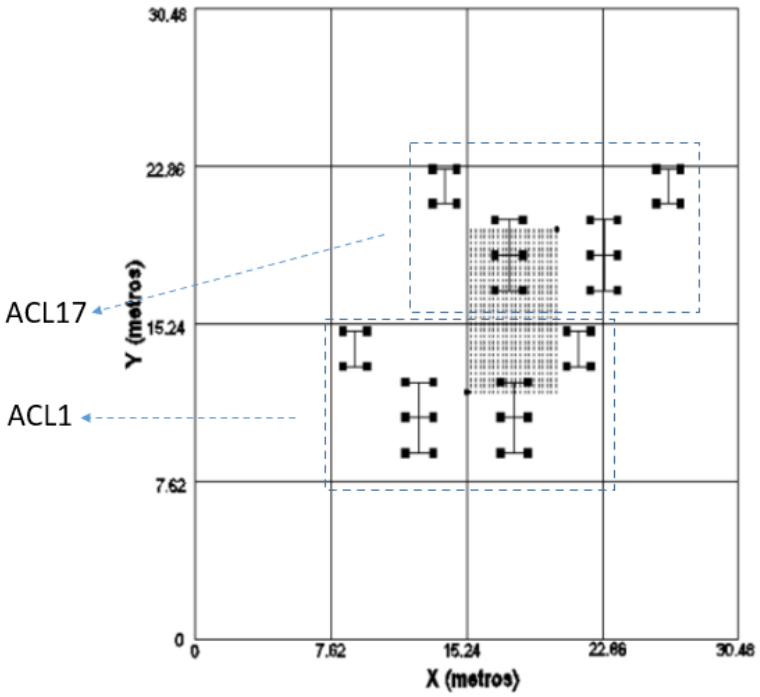

Source: Fonteles (2017)

Figure 3.5 – Demonstration of the ACL 1 to 17 (LP1 to LP17)

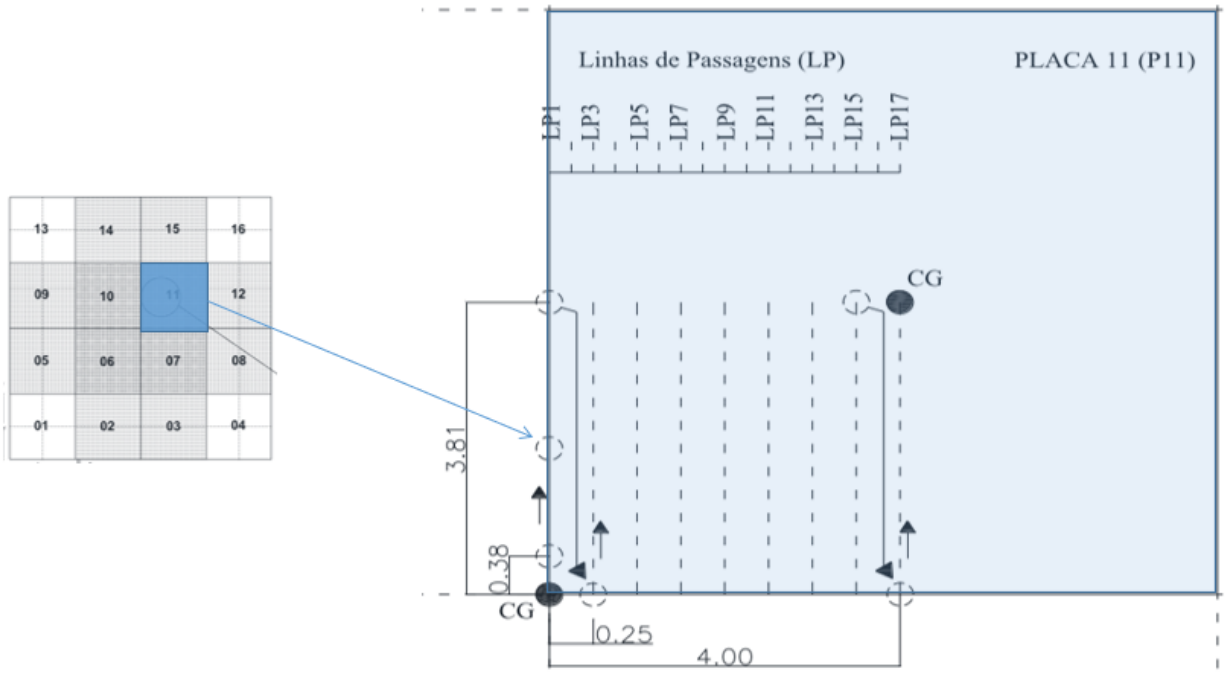

Source: Fonteles (2017)

Figure 3.6 – Graph created by Fonteles (2017) gathering the greatest tensile stresses at whole slab for each application of loading (ACL or LP)

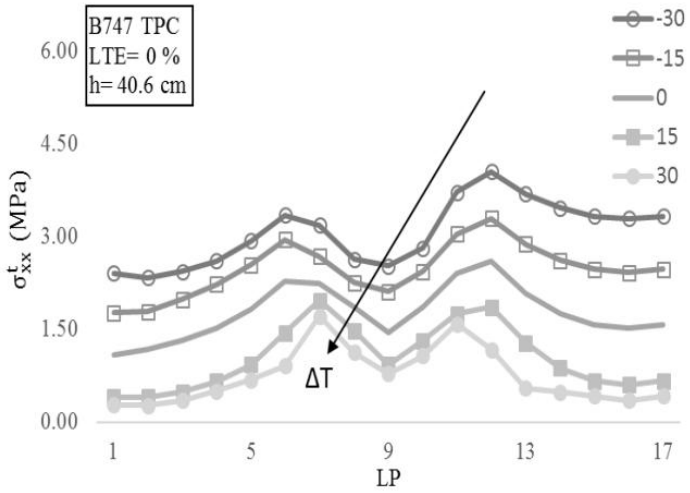

Source: Fonteles (2017)

3.2. CONSTRUCTION OF THE DATASET AND TRAINING THE MODELS

After data extraction, the datasets were organized to be used for training and validating the ML/RF.

3.2.1. Linear Stresses Dataset

The dataset was organized with the FEM results of maximum tensile stress simulated through ILLISLAB simulations provided by Fonteles (2017). Based on those, a dataset was developed in which the input variables are presented in Table 3.2 for the output maximum tensile stress occurred at the top or bottom of the transverse joint ($\sigma_{\Delta T}^{L}$) of the control slab 11. The values between […] are the ones adopted in the simulations, and finite element simulation.

Table 3.2 - Input variables for predicting the maximum linear stress ($\sigma_{\Delta T}^{L}$) in the pavement slab.

Symbol	Description	Adopted values
ξ	Aircraft type	0 (B747) or 1 (A380)
ρ	Tire pressure (MPa)	[1.52; 1.38; 1.03; 0.55]
TB	Stress position in the slab	0 (Top) or 1 (Bottom)
h	Pavement thickness (m)	[0.250; 0.406; 0.508]
LTE	Load transfer efficiency (%)	[0; 85]
ΔT	Linear temperature difference (°C)	[16.67; 8.33; 0; -8.33; -16.67]
ACL	Passing line	[1; …; 17]
ℓ	Radius of relative stiffness (m)	[1.32; 1.44; 2.25]
k	Modulus of subgrade reaction (MPa/m)	[40.7[a]; 13.6[b]]

[a]: used for thickness of 0.406 m; [b]: used for thickness of 0.250 m and 0.508 m.

Source: Author.

With all the combinations between the input variables, it was possible to train the ML/RF by dividing the dataset into 75% for training (119,514 simulations) and 25% for testing (39,838 simulations), total of 159,352 data in the dataset. The algorithm was trained using the Scikit-learn Python library and using 5-fold cross-validation within a Bayesian optimizing algorithm to obtain the best hyperparameters (Table 3.3) that minimized the mean squared error of the cross-validation predictions. The k-fold cross-validation separate randomly the dataset into k folds with same size and use 1 fold as test and the others as training and calculate the error. This process repeats until each fold is used as test and the error of each of them is calculated. Therefore, the error of the model is calculated using the average of the errors (Figure 3.7).

Figure 3.7 – Demonstration of operation of k-fold cross-validation

Source: Savietto (2021)

Table 3.3 – Hyperparameters used for predicting the maximum linear stress ($\sigma_{\Delta T}^{L}$) and the maximum total stress ($\sigma_{\Delta T}^{T}$) in the pavement slab.

Hyperparameters	Values for $\sigma_{\Delta T}^{L}$	Values for $\sigma_{\Delta T}^{T}$
Bootstrap	True	True
Ccp_alpha	0.0	0.0
Criterion	Squared_error	Squared_error
Max_depth	45	35
Max_features	3	2
Max_leaf_nodes	None	None
Max_samples	None	None
Min_impurity_decrease	0.0	0.0
Min_samples_leaf	1	1
Min_samples_split	2	7
Min_weight_fraction_leaf	0.0	0.0
Monotonic_cst	None	None
N_estimators	350	450
N_jobs	None	None
Oob_score	False	False
Random_state	None	None
Verbose	0	0
Warm_start	False	False

Source: Author

3.2.2. Total Stresses Dataset

To build the dataset of self-equilibrating stresses, several statistical analyzes were carried out with data from São Paulo in order to know the characteristic values of each variable, separating them according to the season of the year in which the reading was taken and their time: spring, summer, autumn, winter, day, night and total (all data). To this end, the NOLA parameter was used to characterize the level of nonlinearity of the profiles, this parameter was described by Equation (2.22). Finally, using the different values that could be found using NOLA equation, discovered from the analyses, the dataset used was the one presented in Table 3.4.

Table 3.4 - Input variables for predicting the maximum total stress ($\sigma_{\Delta T}^{T}$) in the pavement slab.

Symbol	Description	Adopted values
ξ	Aircraft type	0 (B747) or 1 (A380)
ρ	Tire pressure (MPa)	[1.52; 1.38; 1.03; 0.55]
TB	Stress position in the slab	0 (Top) or 1 (Bottom)
h	Pavement thickness (m)	[0.250; 0.406; 0.508]
LTE	Load transfer efficiency (%)	[0; 85]
ΔT	Linear temperature difference (°C)	[16.67; 8.33; 0; -8.33; -16.67]
ACL	Passing line	[1; …; 17]
ℓ	Radius of relative stiffness (m)	[1.32; 1.44; 2.25]
k	Modulus of subgrade reaction (MPa/m)	[40.7[a]; 13.6[b]]
NOLA	Non-Linear Area (°C m)	[-3.39, ..., 3.38]

[a]: used for thickness of 0.406 m; [b]: used for thickness of 0.250 m and 0.508 m.

Source: Autor.

With all the combinations between the input variables, it was possible to train the ML/RF by dividing the dataset into 75% for training (510,883 simulations) and 25% for testing (170,295 simulations), total of 681,178 data in the dataset. The algorithm was trained using the Scikit-learn Python library and using 5-fold cross validation within a Bayesian optimizing algorithm to obtain the best hyperparameters (Table 3.3) that minimized the mean squared error of the cross-validation predictions.

3.3. VALIDATION OF THE MODELS AND PERFORMANCE MEASUREMENTS

To validate the Machine Learning technique, initially, several comparison graphs were generated, comparing the data obtained from the ILLISLAB software and those predicted by the proposed ML/RF. Subsequently, performance measurements as the coefficient of determination (R^2), mean absolute errors (MAE), mean square errors (MSE), root mean square errors (RMSE) and absolute residuals (ε_{ab}), were determined for training and testing predictions. Those performance measurements are defined as the Equation (3.7a-e):

$$R^2 = \frac{\sum_{i=1}^{n}\left(\hat{\sigma}_{\Delta T_i} - \bar{\sigma}_{\Delta T}\right)^2}{\sum_{i=1}^{n}\left(\sigma_{\Delta T_i} - \bar{\sigma}_{\Delta T}\right)^2}$$

$$MAE = \frac{\sum_{i=1}^{n}\left|\hat{\sigma}_{\Delta T_i} - \sigma_{\Delta T_i}\right|}{n} \quad (3.7a\text{-}e)$$

$$MSE = \frac{\sum_{i=1}^{n}\left(\hat{\sigma}_{\Delta T_i} - \sigma_{\Delta T_i}\right)^2}{n}$$

$$RMSE = \sqrt{\frac{\sum_{i=1}^{n}\left(\hat{\sigma}_{\Delta T_i} - \sigma_{\Delta T_i}\right)^2}{n}}$$

$$\varepsilon_{ab} = \hat{\sigma}_{\Delta T_i} - \sigma_{\Delta T_i}$$

where n = number of data points; $\hat{\sigma}_{\Delta T_i}$ = maximum tensile stress predicted by the proposed ML/RF ($\hat{\sigma}_{\Delta T}$); $\sigma_{\Delta T_i}$ = maximum tensile stress observed in the dataset ($\sigma_{\Delta T}$ predicted by FE simulation); and $\bar{\sigma}_{\Delta T}$ = average of $\sigma_{\Delta T_i}$ values.

4. RESULTS AND DISCUSSIONS

In this section, the results obtained with the proposed ML/RF models is presented on two subsections: direct comparison with ILLISLAB and performance analysis of trained and tested machine learning models. In addition, measurements obtained from the analysis of temperature data from São Paulo will be presented.

4.1. LINEAR STRESS

4.1.1. Direct Comparison Between Machine Learning Final Model and ILLISLAB Simulations

Comparisons were made by plotting the original data simulated by Fonteles (2017) and the tensile stresses predicted by the proposed machine learning ML/RF model for different configurations, especially different temperature differential though the slab´s thickness (ΔT) and passing lines position of the landing gear (ACLs). The plots can be seen from Figure 4.1 to Figure 4.6, being grouped according to the aircraft type (A380 and B747) and the slab´s thickness (0.250, 0.406, and 0.508).

Figure 4.1 - Comparison between proposed machine learning ML/RF (continuous line) and ILLISLAB (dashed line) predictions of maximum linear tensile stress ($\sigma_{\Delta T}^{L}$) for different passing lines (ACL) for A380, h = 0.250m, Top stress: a) LTE = 0%, b) LTE = 85%; Bottom stress: c) LTE = 0%, d) LTE = 85%

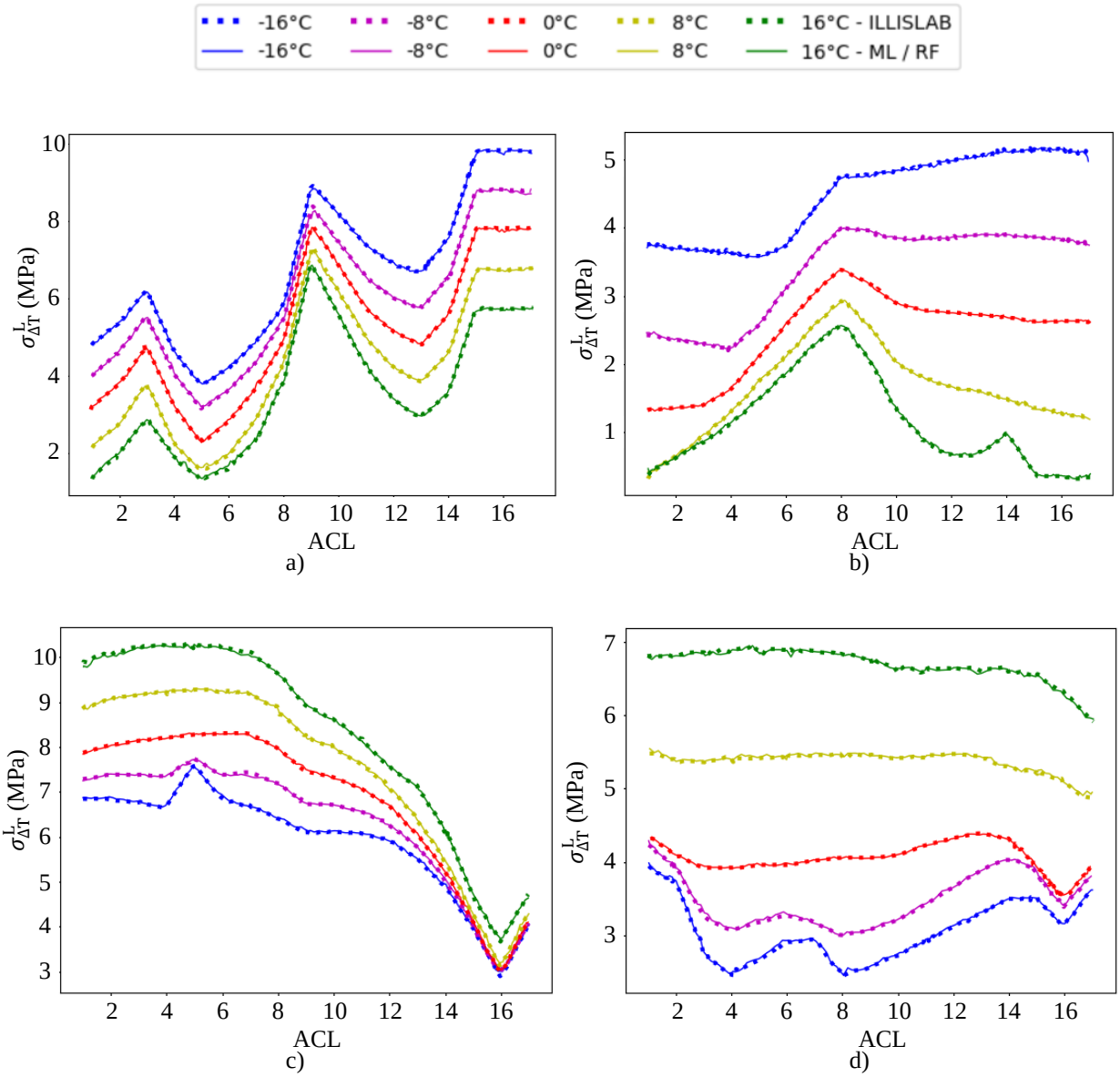

Source: Author.

Figure 4.2 - Comparison between proposed machine learning ML/RF (continuous line) and ILLISLAB (dashed line) predictions of maximum linear tensile stress ($\sigma_{\Delta T}^{L}$) for different passing lines (ACL) for A380, h = 0.406m, Top stress: a) LTE = 0%, b) LTE = 85%; Bottom stress: c) LTE = 0%, d) LTE = 85%

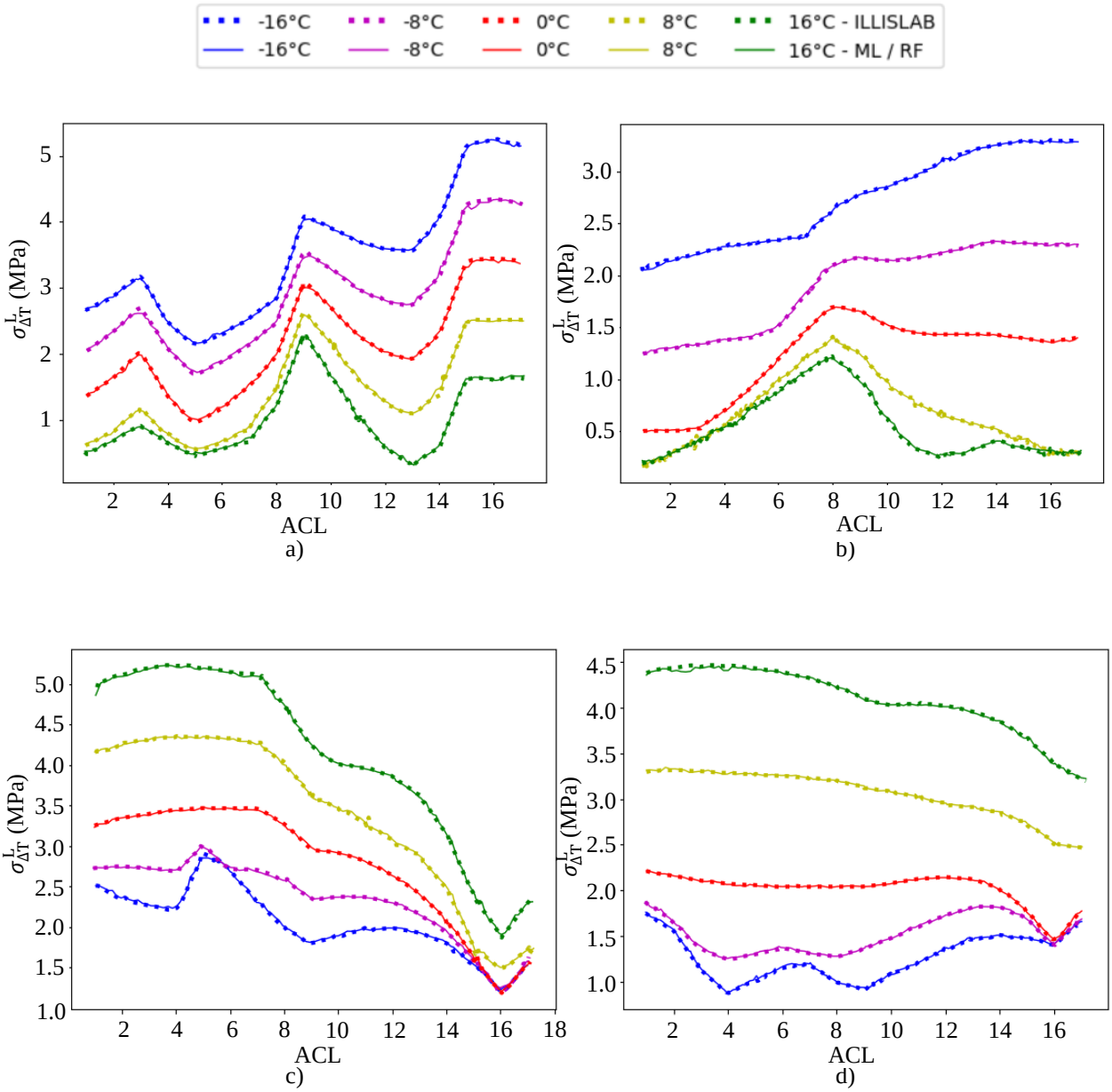

Source: Author.

Figure 4.3 - Comparison between proposed machine learning ML/RF (continuous line) and ILLISLAB (dashed line) predictions of maximum linear tensile stress ($\sigma_{\Delta T}^{L}$) for different passing lines (ACL) for A380, h = 0.508m, Top stress: a) LTE = 0%, b) LTE = 85%; Bottom stress: c) LTE = 0%, d) LTE = 85%

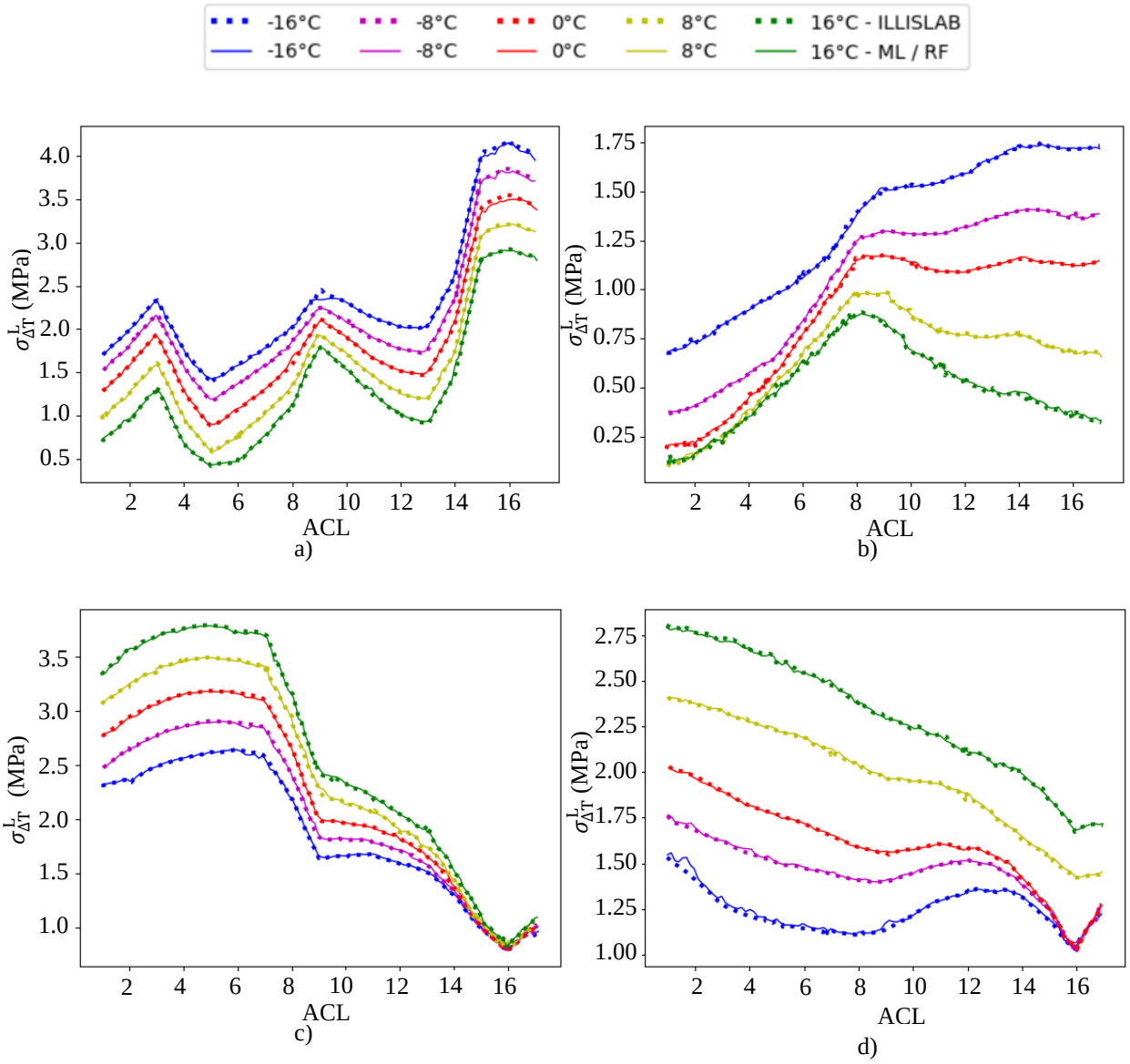

Source: Author.

Figure 4.4 - Comparison between proposed machine learning ML/RF (continuous line) and ILLISLAB (dashed line) predictions of maximum linear tensile stress ($\sigma^{L}_{\Delta T}$) for different passing lines (ACL) for B747, h = 0.250m, Top stress: a) LTE = 0%, b) LTE = 85%; Bottom stress: c) LTE = 0%, d) LTE = 85%

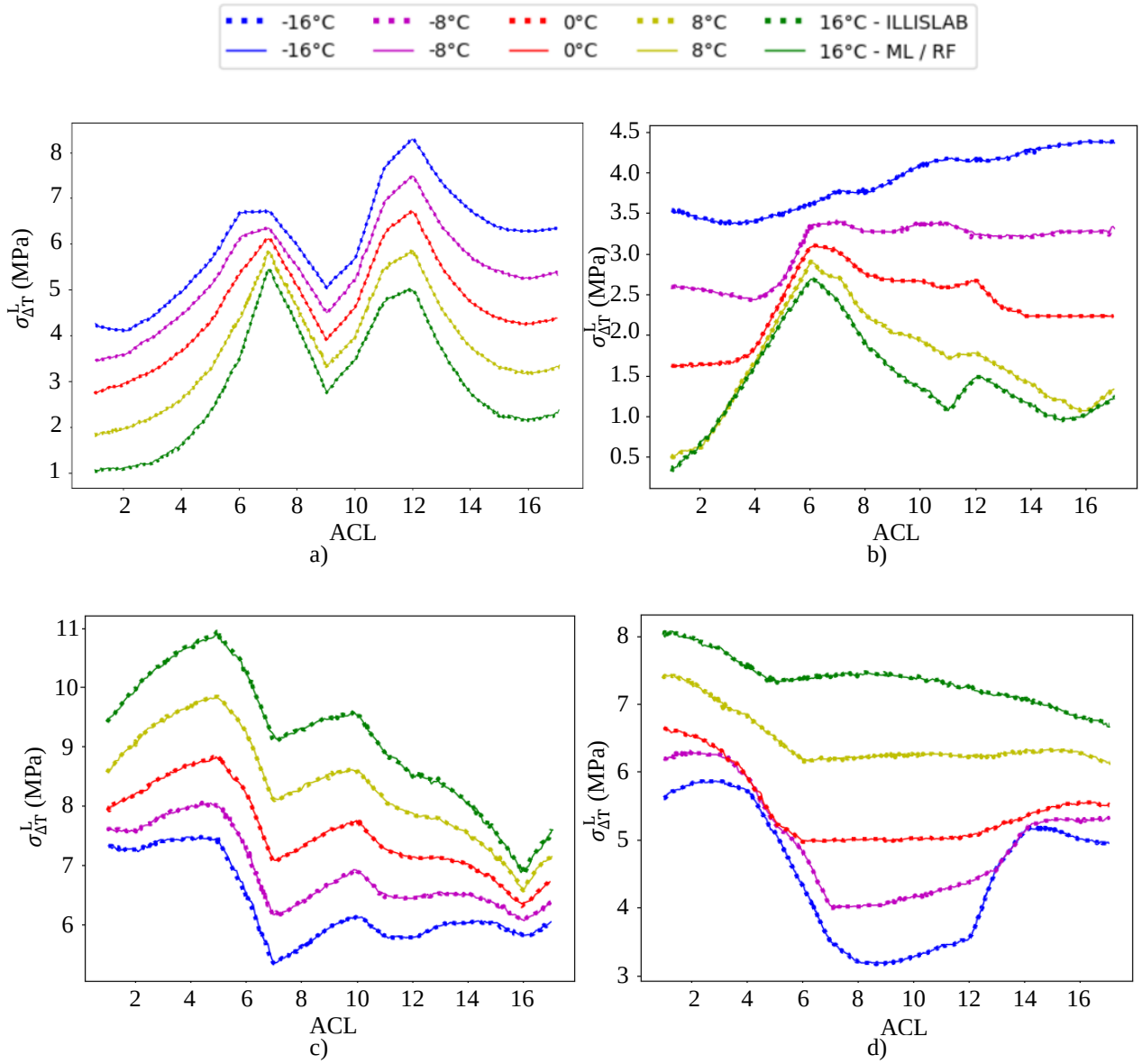

Source: Author.

Figure 4.5 - Comparison between proposed machine learning ML/RF (continuous line) and ILLISLAB (dashed line) predictions of maximum linear tensile stress ($\sigma_{\Delta T}^{L}$) for different passing lines (ACL) for B747, h = 0.406m, Top stress: a) LTE = 0%, b) LTE = 85%; Bottom stress: c) LTE = 0%, d) LTE = 85%

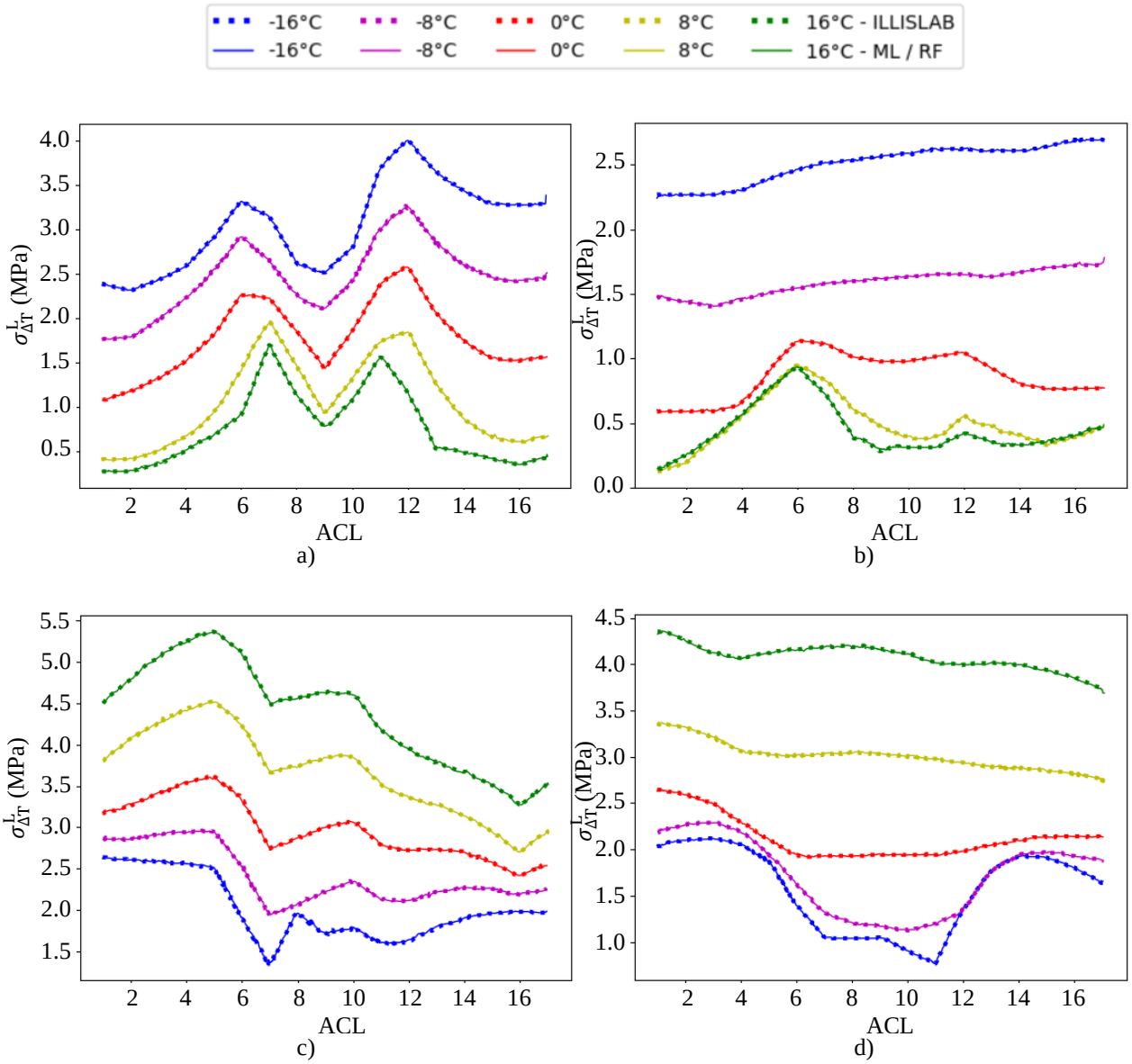

Source: Author.

Figure 4.6 - Comparison between proposed machine learning ML/RF (continuous line) and ILLISLAB (dashed line) predictions of maximum linear tensile stress ($\sigma^{L}_{\Delta T}$) for different passing lines (ACL) for B747, h = 0.508m, Top stress: a) LTE = 0%, b) LTE = 85%; Bottom stress: c) LTE = 0%, d) LTE = 85%

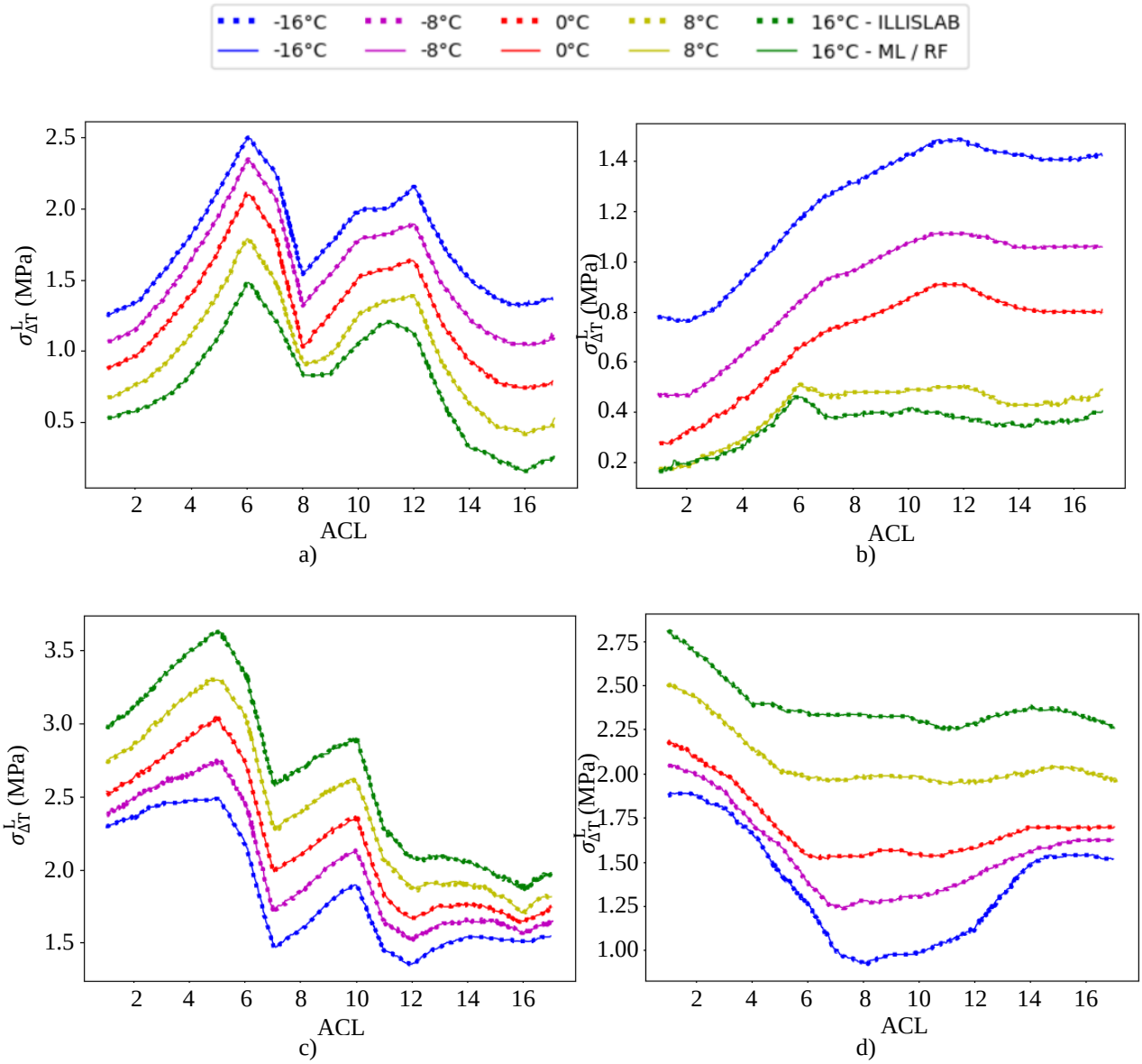

Source: Author.

The results presented by the figures showed a very good agreement between the proposed ML/RF predictions and the original ILLISLAB simulated tensile stresses (top and bottom surface) for all the configurations with different aircraft type loading, slab´s thickness, temperature differentials and load transfer efficiency. The ML/RF showed very good agreement even in strong variation of the distribution of tensile stresses along the passing lines, for example, see the spikily tensile stress variations around ACL 8 when considering

LTE=0% (subfigures a) and c)). Note also that the proposed model is able to predict tensile stresses with negative, positive, and null temperature differential across the thickness.

4.1.2. Performance of Training and Test

The performance of the ML/RF can be qualitatively assessed with the comparison presented in Figure 4.7, which visually the ILLISLAB predictions $\sigma_{\Delta T}^{L}$ and the data predicted by the proposed ML/RF model $\hat{\sigma}_{\Delta T}^{L}$ for both training and testing datasets. The ML/RF predicted values were extremely close to the line of equality (45° degrees line) demonstrating an almost perfect equality between the ILLISLAB and machine learning predictions. This extreme similarity could be an indicator of overfitting of the data by the machine learning model, however, the same equality of predictions can be seen on the testing plot where all those data were unseen by the training phase, which excludes overfitting during model training.

Also note that both ILLISLAB and ML/RF predicted very high tensile stresses reaching up to 12 MPa which is far off the range accepted in pavement design. Those predicted values are from extreme combinations such as high values for tire pressure and $|\Delta T|$ combined with lower values of thickness, modulus of subgrade reaction and load transfer efficiency. Those combinations are part of the dataset to allow a comprehensive machine learning model able to accurate predict possible extreme conditions to be discarded during the design phase.

Figure 4.7 - Maximum tensile stresses obtained with ILLISLAB ($\sigma_{\Delta T}^{L}$) and predicted with ML/RF ($\hat{\sigma}_{\Delta T}^{L}$) for the datasets: a) Training; b) Testing

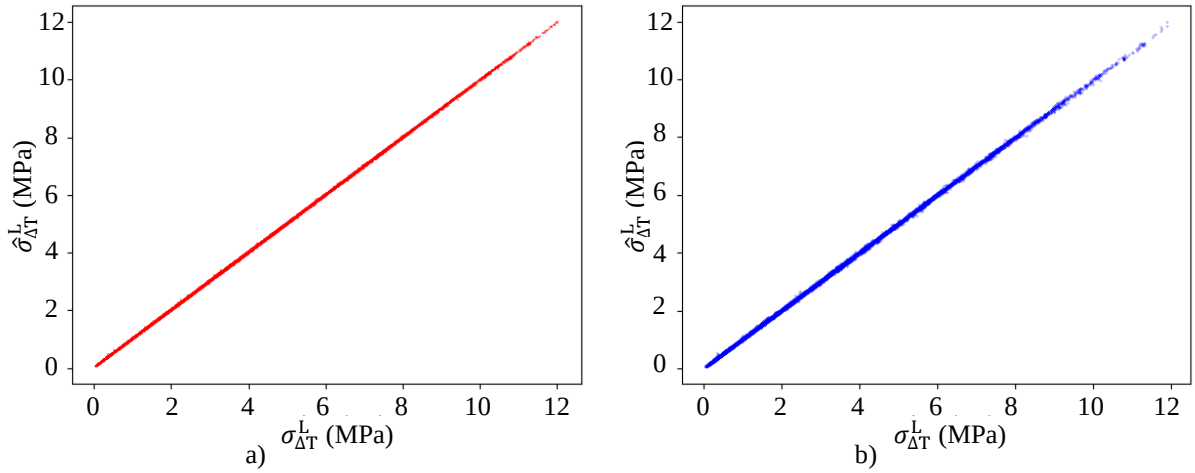

Source: Author.

Table 4.1 further confirms the high accuracy of the ML/RF predictions and effectivity of the trained algorithm showed high R^2 and low values for the error performance measurements (MAE, MSE, and RMSE) for both training and testing datasets. Note that for all error measurements, the performance of the testing presented higher errors than the training, indicating that the overfitting did not occur during training. The good performance presented by the can be attributed to the Random Forest algorithm be able to very accurately model the data based on the input variable of Table 3.2.

Table 4.1 - Performance measurements with ML/RF for linear tensile stresses

Dataset	R^2 (%)	MAE (MPa)	MSE (MPa^2)	RMSE (MPa)
Training	99.99	4.47e-3	6.20e-5	7.87e-3
Testing	99.99	1.09e-2	3.60e-4	1.90e-2

Source: Autor.

Figure 4.8 presents histograms of absolute residuals (ε_{ab}^{L}) which shows those errors values with its number of occurrences for both training and testing. Both histograms show most of the errors were concentrated between -0.05 MPa and 0.05 MPa, with the highest concentration occurring many close to 0 as expected for an adequate machine learning model.

Figure 4.8 - Histogram of absolute residuals for linear tensile stresses (ε_{ab}^{L}) for the dataset: a) Training; b) Testing

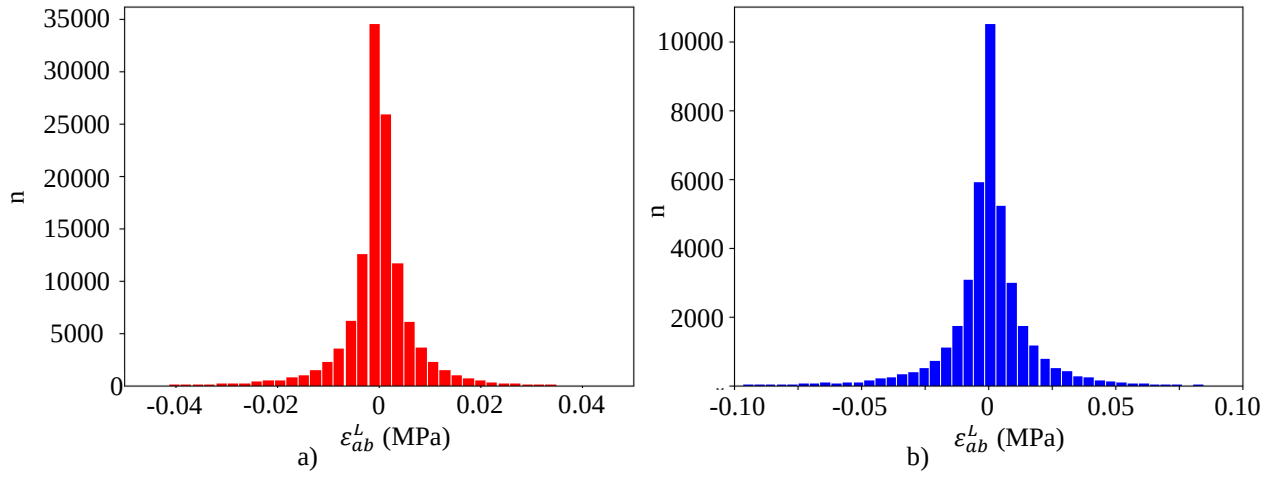

Source: Author.

The bar charts presented in the Figure 4.9 show the ε_{ab}^{L} with the observed tensile stresses obtained with ILLISLAB for both the training and testing datasets which shows the errors distributed over the values of the simulated stress. In the tested dataset (Figure 4.9b), which were unseen by the algorithm during training, only a few cases $\varepsilon_{ab}^{L} > 0.20\,MPa$, however those cases are on the range $\sigma_{\Delta T}^{L} > 6\,MPa$. As desired, the bar's distribution does not show any trend of accumulating higher ε_{ab}^{L} in specific ranges of $\sigma_{\Delta T}^{L}$ for both training and testing sets.

Figure 4.9 – Linear tensile stresses obtained with ILLISLAB ($\sigma_{\Delta T}^{L}$) and absolute residuals (ε_{ab}^{L}) for the database: a) Training; b) Testing

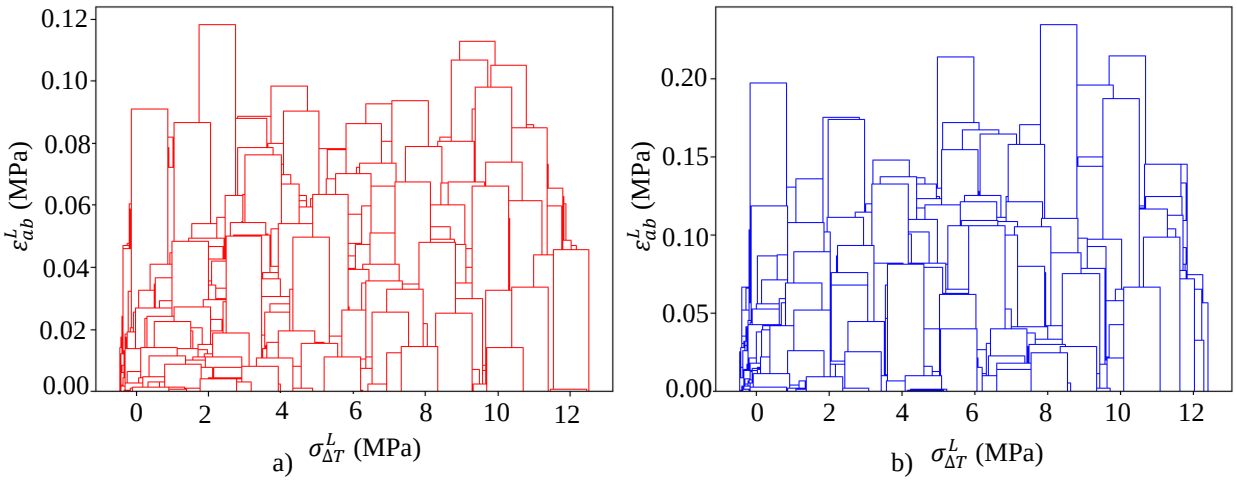

Source: Author.

Probability plots of ε_{ab}^{L} for both training and testing datasets are presented in Figure 4.10, relating the theoretical quantity (TQ), represented by standard deviations of ε_{ab}^{L}, with the ordered ε_{ab}^{L} data (OV). The figure shows that the ε_{ab}^{L} follows a normal distribution with the range of ± 2 standard deviations, but deviated from normality beyond that point which are the rare combinations among the input combinations of Table 3.2. Even on those ranges, the proposed ML/RF show small absolute errors.

Figure 4.10 - Probability plots with absolute residuals (ε_{ab}^{L}) for the database: a) Training; b) Testing

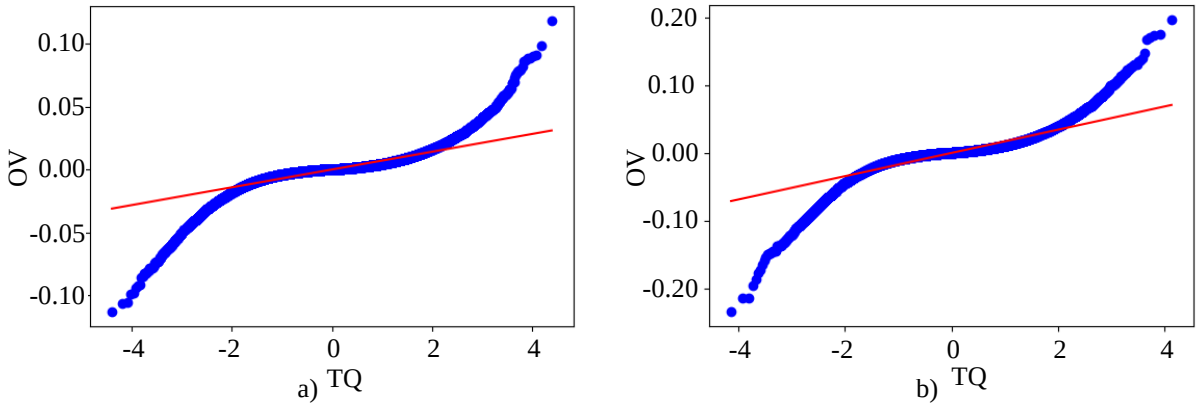

Source: Author.

4.2. TOTAL STRESS

4.2.1. Direct Comparison Between Machine Learning Final Model and ILLISLAB Simulations

Comparisons were made by plotting the original data simulated by Fonteles (2017) added to the self-equilibrating stresses obtained through the Equation (2.26) using the $T_{m_{Q95}}$ and ω_{Q05} from the day and night scenarios of São Paulo, and the tensile stresses predicted by the proposed machine learning ML/RF model for different configurations, especially different temperature differential though the slab´s thickness (ΔT) and passing lines position of the landing gear (ACLs). The plots can be seen from Figure 4.11 to Figure 4.16, being grouped according to the aircraft type (A380 and B747), the slab´s thickness (0.250, 0.406, and 0.508), the average temperature on the slab (36.16 and 33.26), and the level of nonlinearity (-0.134 and -0.036).

Figure 4.11 - Comparison between proposed machine learning ML/RF (continuous line) and ILLISLAB (dashed line) predictions of maximum total tensile stress ($\sigma_{\Delta T}^{T}$) for different passing lines (ACL) for h = 0.250m, LTE = 85% and $NOLA$ = -0.808. B747: a) Top stress, b) Bottom stress; A380: c) Top stress, d) Bottom stress

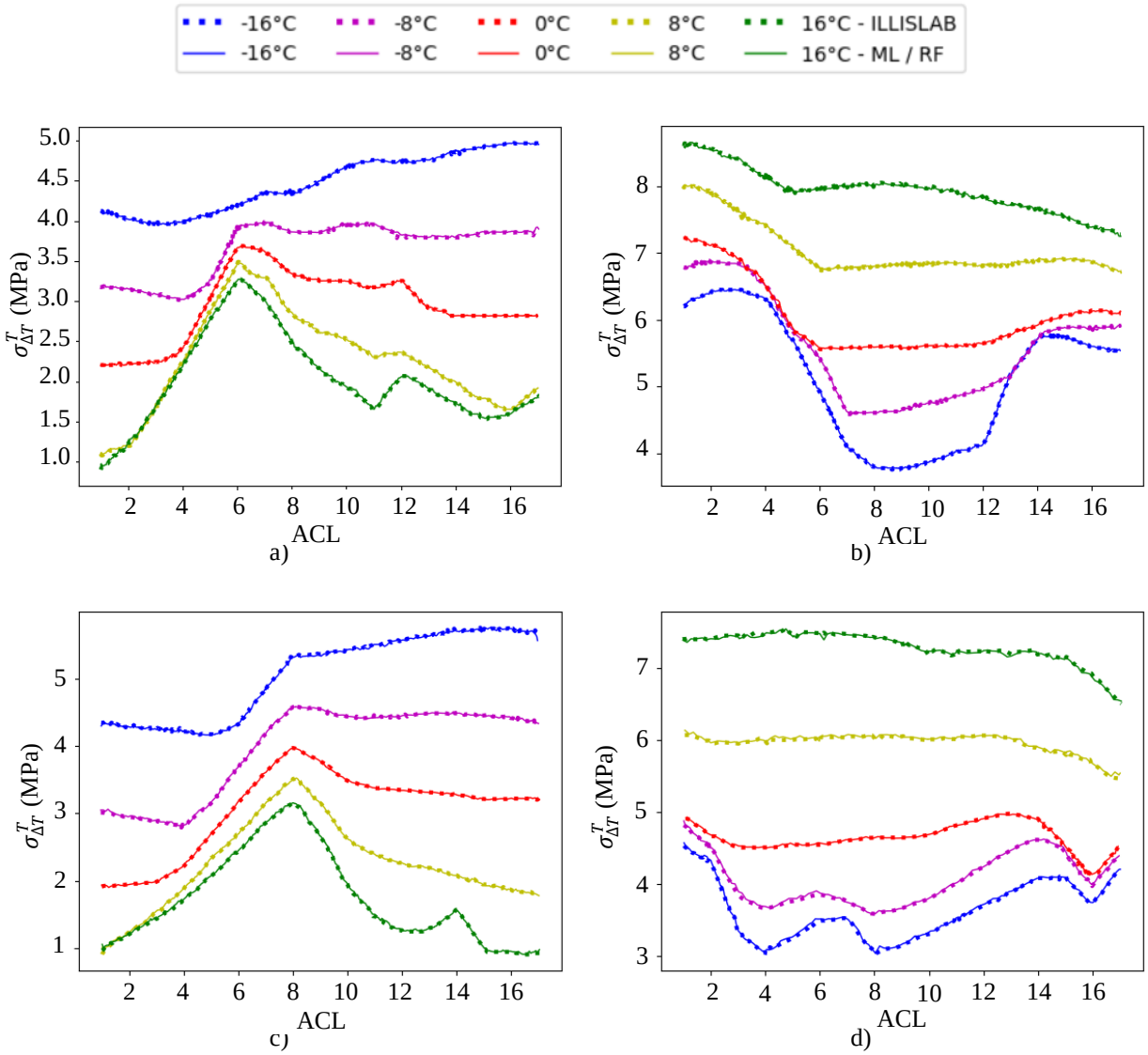

Source: Author.

Figure 4.12 - Comparison between proposed machine learning ML/RF (continuous line) and ILLISLAB (dashed line) predictions of maximum total tensile stress ($\sigma_{\Delta T}^{T}$) for different passing lines (ACL) for h = 0.406m, LTE = 85% and $NOLA$ = -1.312. B747: a) Top stress, b) Bottom stress; A380: c) Top stress, d) Bottom stress

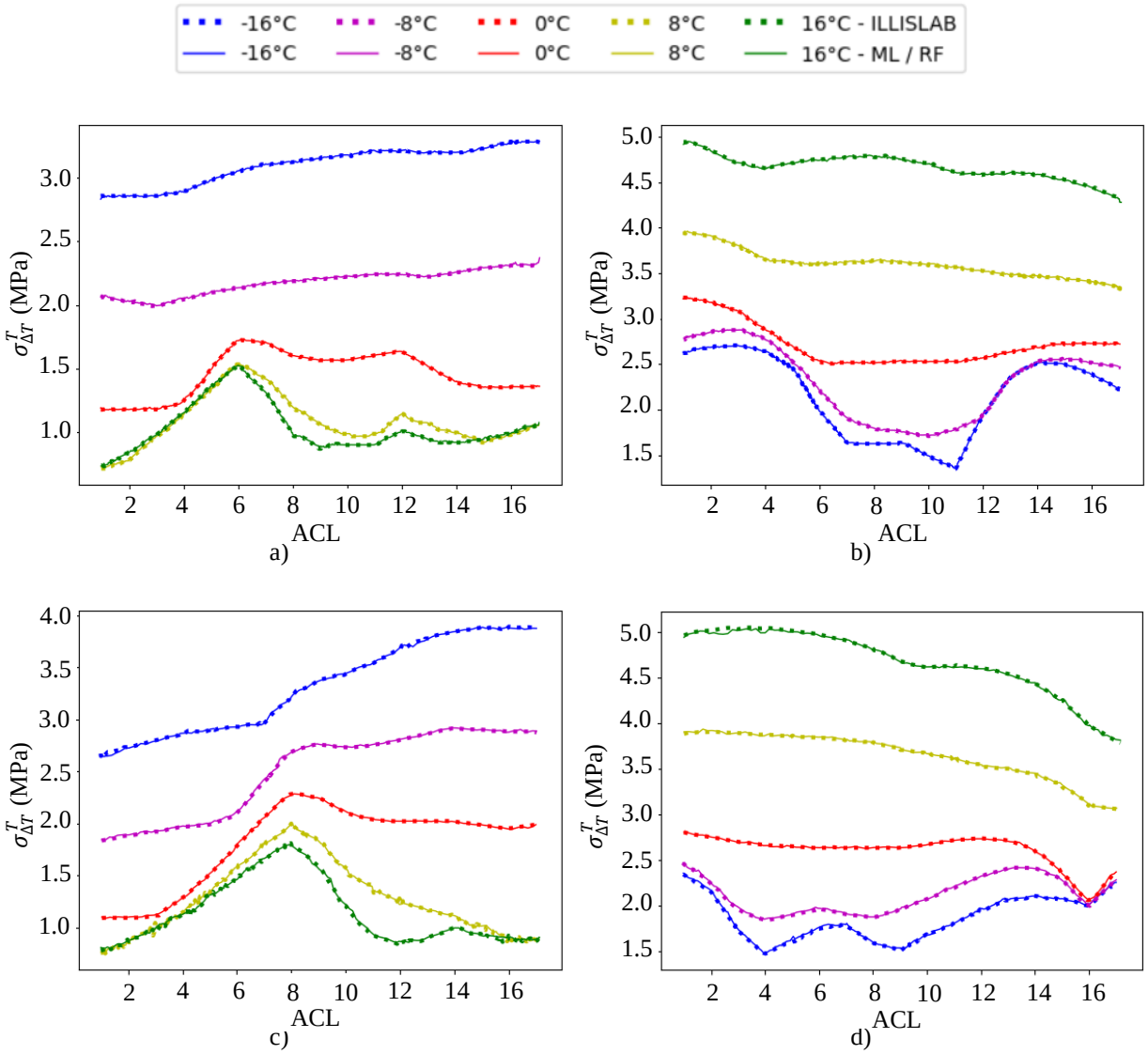

Source: Author.

Figure 4.13 - Comparison between proposed machine learning ML/RF (continuous line) and ILLISLAB (dashed line) predictions of maximum total tensile stress ($\sigma_{\Delta T}^{T}$) for different passing lines (ACL) for h = 0.508m, LTE = 85% and $NOLA$ = -1.641. B747: a) Top stress, b) Bottom stress; A380: c) Top stress, d) Bottom stress

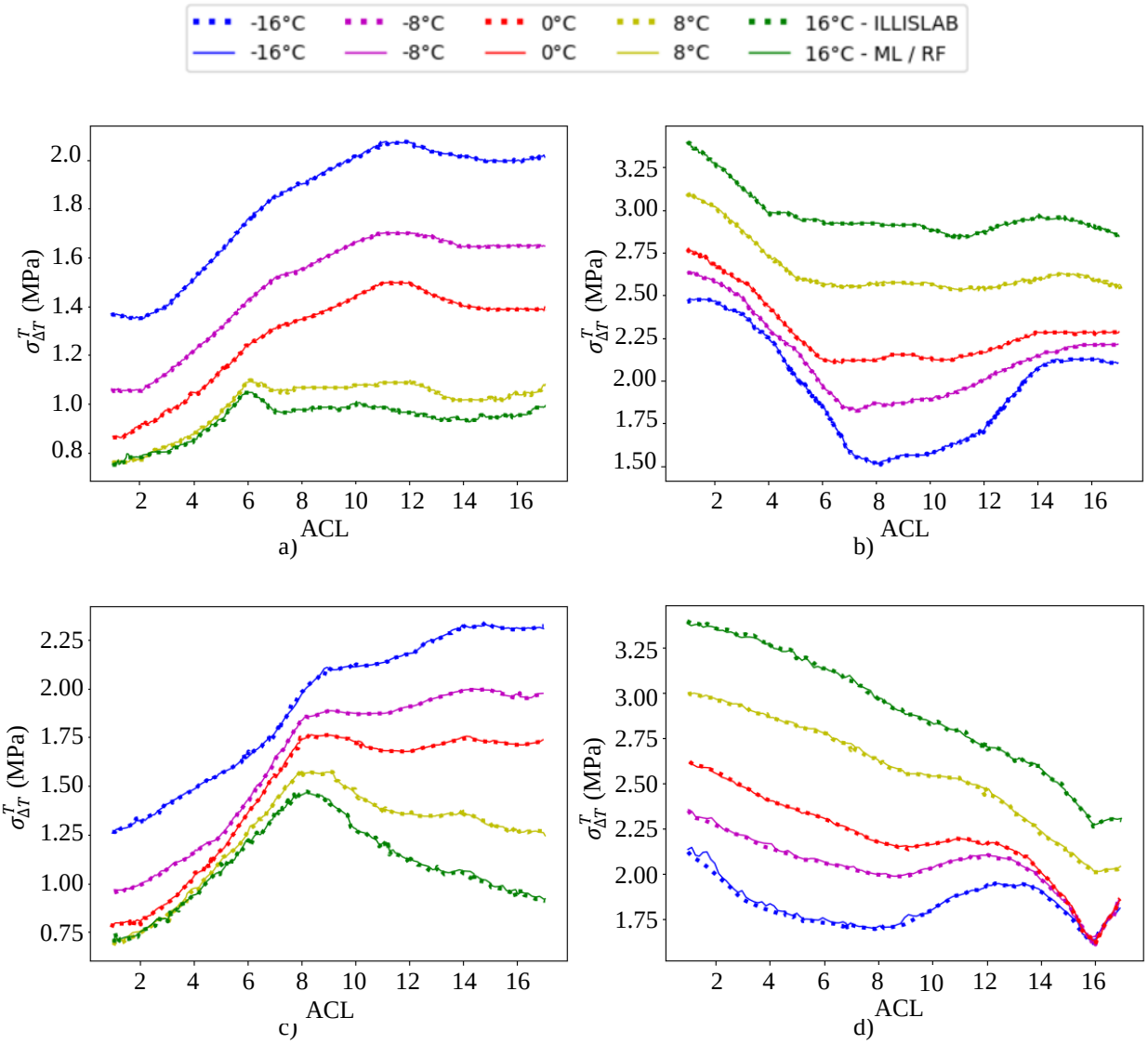

Source: Author.

Figure 4.14 - Comparison between proposed machine learning ML/RF (continuous line) and ILLISLAB (dashed line) predictions of maximum total tensile stress ($\sigma_{\Delta T}^{T}$) for different passing lines (ACL) for h = 0.250m, LTE = 85% and $NOLA$ = -0.200. B747: a) Top stress, b) Bottom stress; A380: c) Top stress, d) Bottom stress

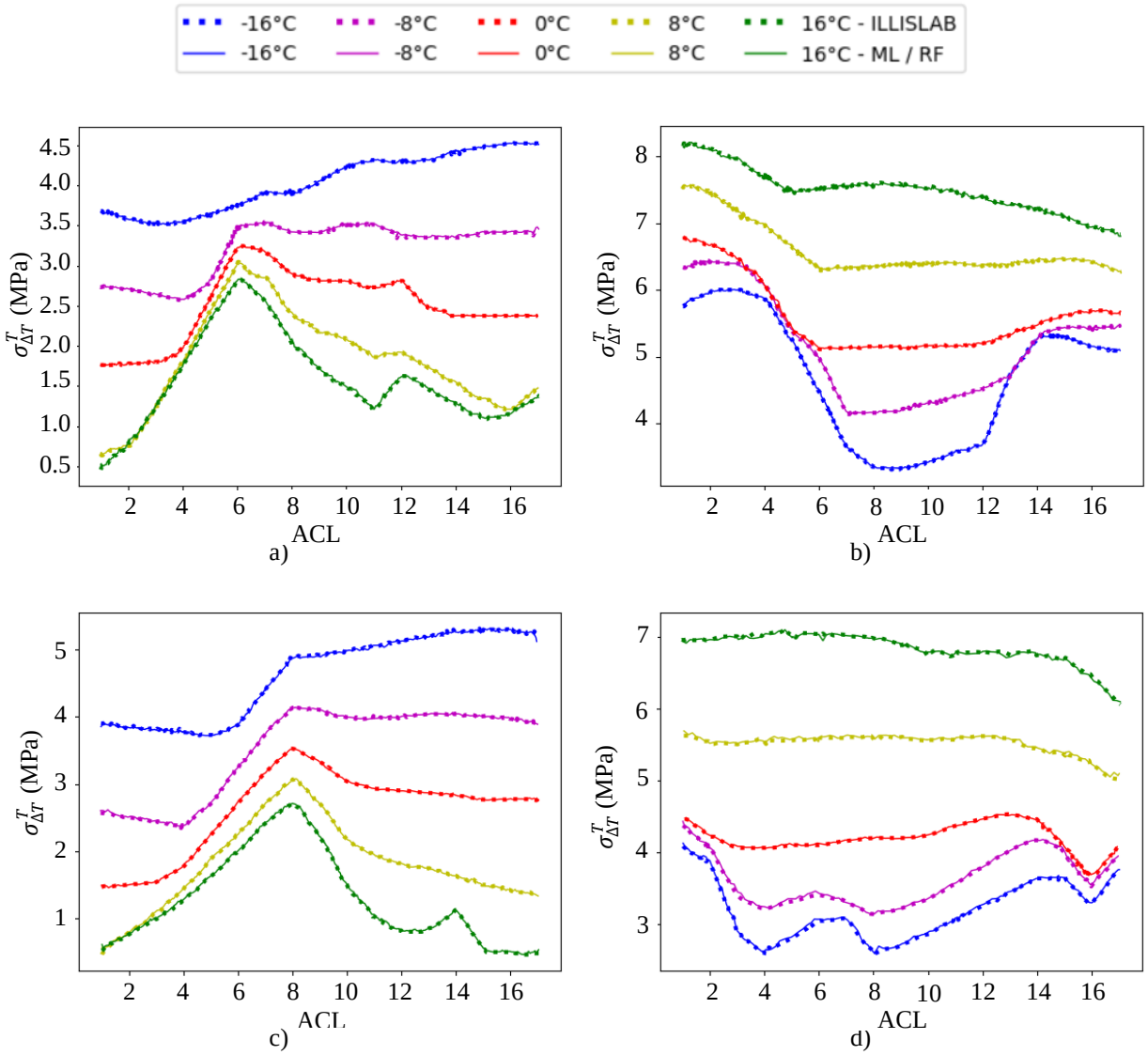

Source: Author.

Figure 4.15 - Comparison between proposed machine learning ML/RF (continuous line) and ILLISLAB (dashed line) predictions of maximum total tensile stress ($\sigma_{\Delta T}^{T}$) for different passing lines (ACL) for h = 0.406m, LTE = 85% and $NOLA$ = -0.324. B747: a) Top stress, b) Bottom stress; A380: c) Top stress, d) Bottom stress

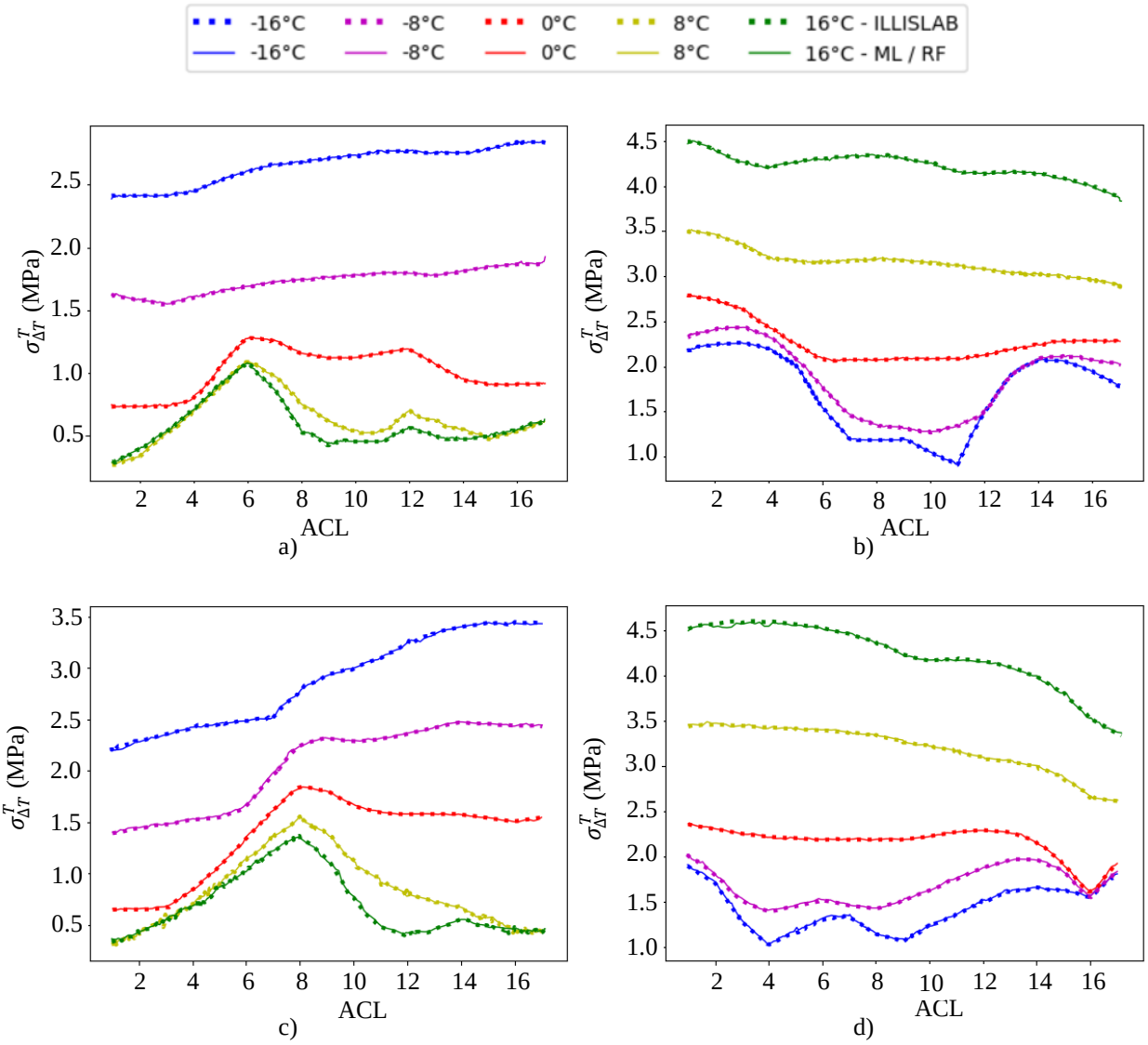

Source: Author.

Figure 4.16 - Comparison between proposed machine learning ML/RF (continuous line) and ILLISLAB (dashed line) predictions of maximum total tensile stress ($\sigma_{\Delta T}^{T}$) for different passing lines (ACL) for h = 0.508m, LTE = 85% and $NOLA$ = -0.406. B747: a) Top stress, b) Bottom stress; A380: c) Top stress, d) Bottom stress

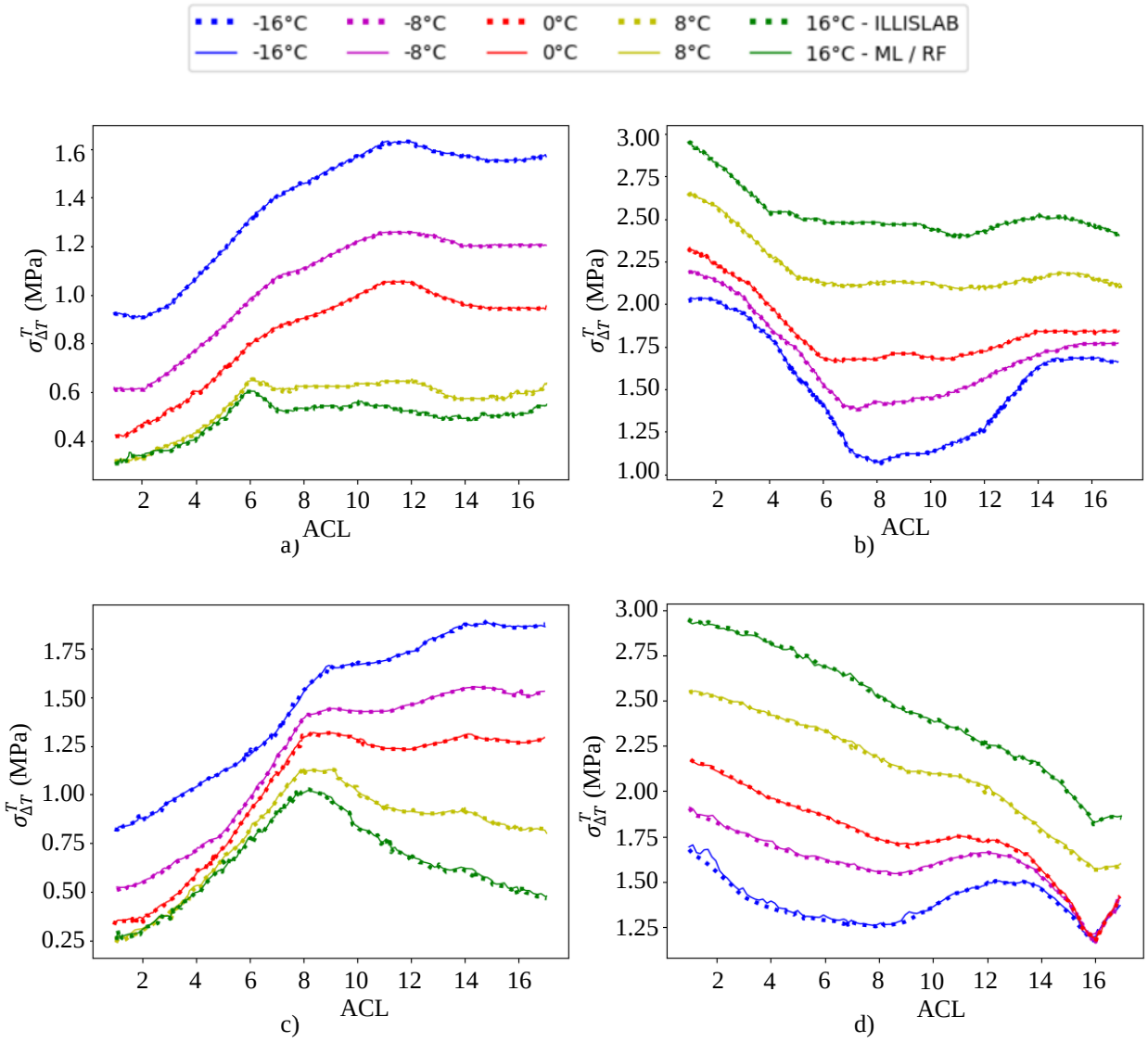

Source: Author.

The results presented by the figures showed a very good agreement between the proposed ML/RF predictions and the original ILLISLAB simulated tensile stresses (top and bottom surface) for all the configurations with different aircraft type loading, slab´s thickness, temperature differentials, load transfer efficiency, average temperature and level of nonlinearity. The ML/RF showed very good agreement even in strong variation of the distribution of tensile stresses along the passing lines. Note also that the proposed model is able to predict tensile stresses with negative, positive, and null temperature differential across

the thickness. In addition to this, comparing different thicknesses and same LTE, is possible to notice that the nonlinearity with respect to passing lines (ACL) and temperatures.

4.2.2. Performance of Training and Test

The performance of the ML/RF can be qualitatively assessed with the comparison presented in Figure 4.17 - , which visually the ILLISLAB predictions $\sigma_{\Delta T}^{T}$ and the data predicted by the proposed ML/RF model $\hat{\sigma}_{\Delta T}^{T}$ for both training and testing datasets. The ML/RF predicted values were extremely close to the line of equality (45° degrees line) demonstrating an almost perfect equality between the ILLISLAB and machine learning predictions. This extreme similarity could be an indicator of overfitting of the data by the machine learning model, however, the same equality of predictions can be seen on the testing plot where all those data were unseen by the training phase, which excludes overfitting during model training.

Also note that both ILLISLAB and ML/RF predicted very high tensile stresses reaching up to 12 MPa which is far off the range accepted in pavement design. Those predicted values are from extreme combinations such as high values for tire pressure and |ΔT| combined with lower values of thickness, modulus of subgrade reaction and load transfer efficiency. Those combinations are part of the dataset to allow a comprehensive machine learning model able to accurate predict possible extreme conditions to be discarded during the design phase.

Figure 4.17 - Maximum tensile stresses obtained with ILLISLAB ($\sigma_{\Delta T}^{T}$) and predicted with ML/RF ($\hat{\sigma}_{\Delta T}^{T}$) for the datasets: a) Training; b) Testing

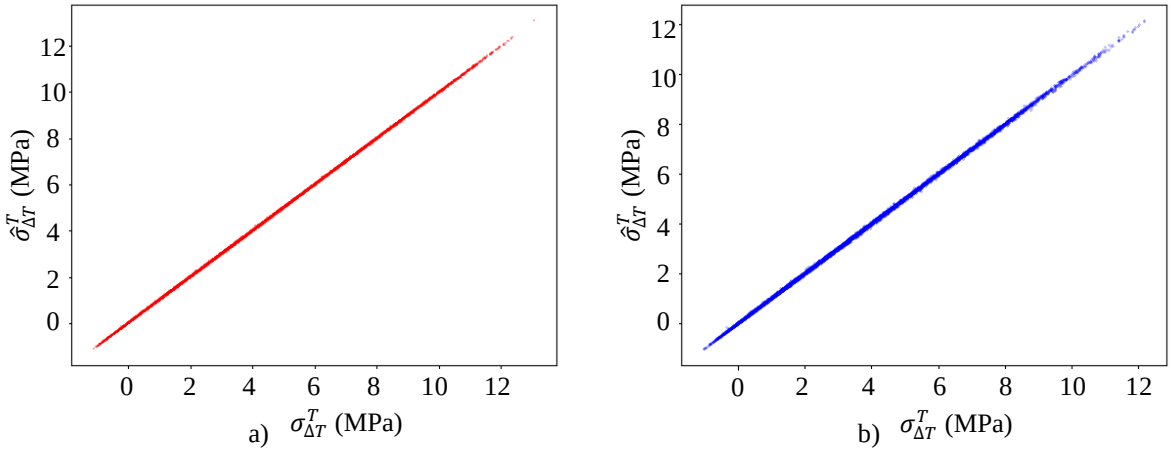

Source: Author.

Table 4.2 further confirms the high accuracy of the ML/RF predictions and effectivity of the trained algorithm showed high R^2 and low values for the error performance measurements (MAE, MSE, and RMSE) for both training and testing datasets. Note that for all error measurements, the performance of the testing presented higher errors than the training, indicating that the overfitting did not occur during training. The good performance presented by the can be attributed to the Random Forest algorithm be able to very accurately model the data based on the input variable of Table 3.4.

Table 4.2 - Performance measurements with ML/RF for total tensile stresses.

Dataset	R^2 (%)	MAE (MPa)	MSE (MPa^2)	RMSE (MPa)
Training	99.99	4.49e-3	6.21e-5	7.88e-3
Testing	99.99	1.09e-2	3.60e-4	1.90e-2

Source: Author.

Figure 4.18 presents histograms of absolute residuals (ε_{ab}^{T}) which shows those errors values with its number of occurrences for both training and testing. Both histograms show most of the errors were concentrated between -0.05 MPa and 0.05 MPa, with the highest concentration occurring many close to 0 as expected for an adequate machine learning model.

Figure 4.18 - Histogram of absolute residuals (ε_{ab}^{T}) for the dataset: a) Training; b) Testing

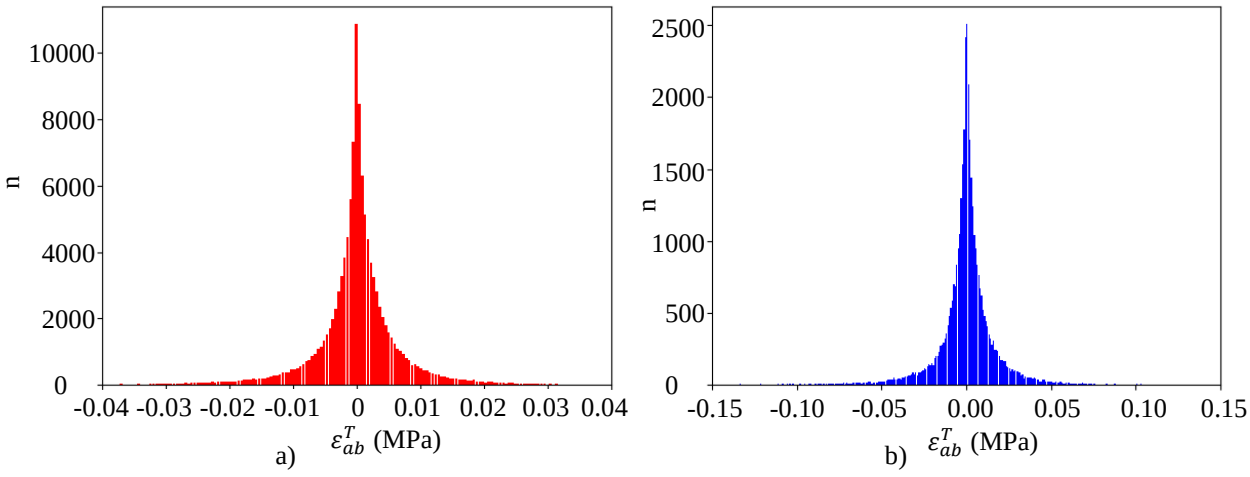

Source: Author.

The bar charts presented in the Figure 4.19 show the ε_{ab}^{T} with the observed stresses obtained with ILLISLAB for both the training and testing datasets which shows the errors

distributed over the values of the simulated stress. In the tested dataset (Figure 4.19b), which were unseen by the algorithm during training, only a few cases $\varepsilon_{ab}^{T} > 0.20\,MPa$, however those cases are on the range $\sigma_{\Delta T}^{T} > 6\,MPa$. As desired, the bar's distribution does not show any trend of accumulating higher ε_{ab}^{T} in specific ranges of $\sigma_{\Delta T}^{T}$ for both training and testing sets.

Figure 4.19 - Total tensile stresses obtained with ILLISLAB ($\sigma_{\Delta T}^{T}$) and absolute residuals (ε_{ab}^{T}) for the database: a) Training; b) Testing

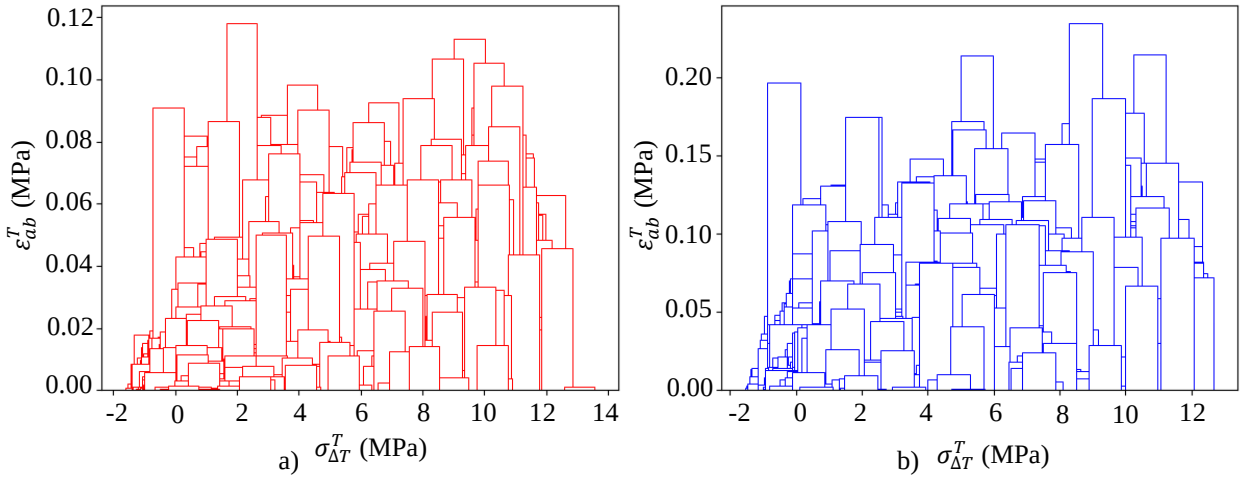

Source: Author.

Probability plots of ε_{ab}^{T} for both training and testing datasets are presented in Figure 4.20, relating the theoretical quantity (TQ), represented by standard deviations of ε_{ab}^{T}, with the ordered ε_{ab}^{T} data (OV). The figure shows that the ε_{ab}^{T} follows a normal distribution with the range of ± 2 standard deviations, but deviated from normality beyond that point which are the rare combinations among the input combinations of Table 3.4. Even on those ranges, the proposed ML/RF show small absolute errors.

Figure 4.20 - Probability plots with absolute residuals (ε_{ab}^{T}) for the database: a) Training; b) Testing

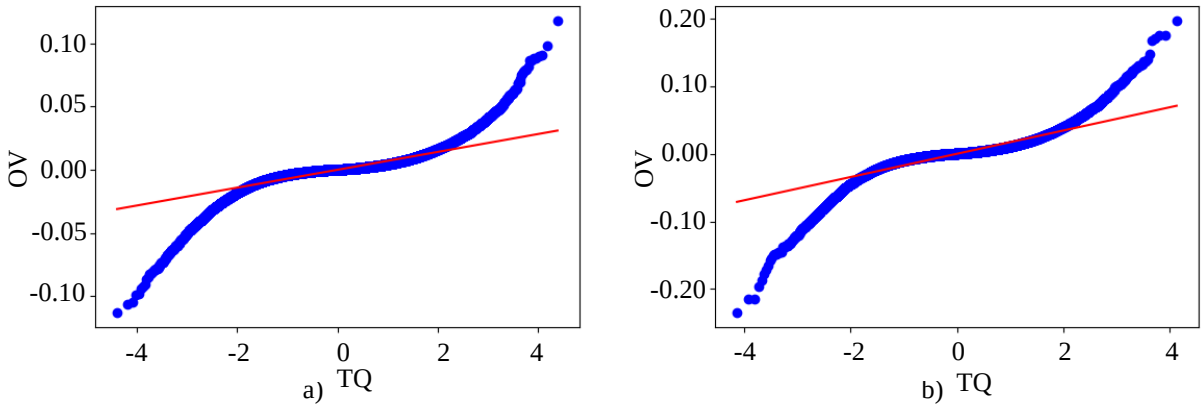

Source: Author.

4.3. ANALYSIS OF SÃO PAULO TEMPERATURE DATA

Severi (2002) used an experimental track composed of 15 concrete slabs with different sizes (Figure 4.21) instrumented with thermal resistors built at the Polytechnic School of the University of São Paulo to obtain temperature profile data. The resistors were installed in strategic locations (in the center and at the edge of each slab) (Figure 4.22) positioned at 2.00 cm, 7.25, 12.50 cm, 17.75 cm and 19.75 cm from the top of the pavement. Data were collected between October 1999 and February 2001, totaling 190 reading days, 74 readings on spring days, 39 on summer days, 43 in autumn and 34 in winter. The readings were taken at different times of the day, thus obtaining graphs such as Figure 4.23 constructed with Severi (2002)'s data, which shows the temperature at each depth for each reading time:

Figure 4.21 – Layout of concrete slabs built as experimental track at the Polytechnic School of the University of São Paulo

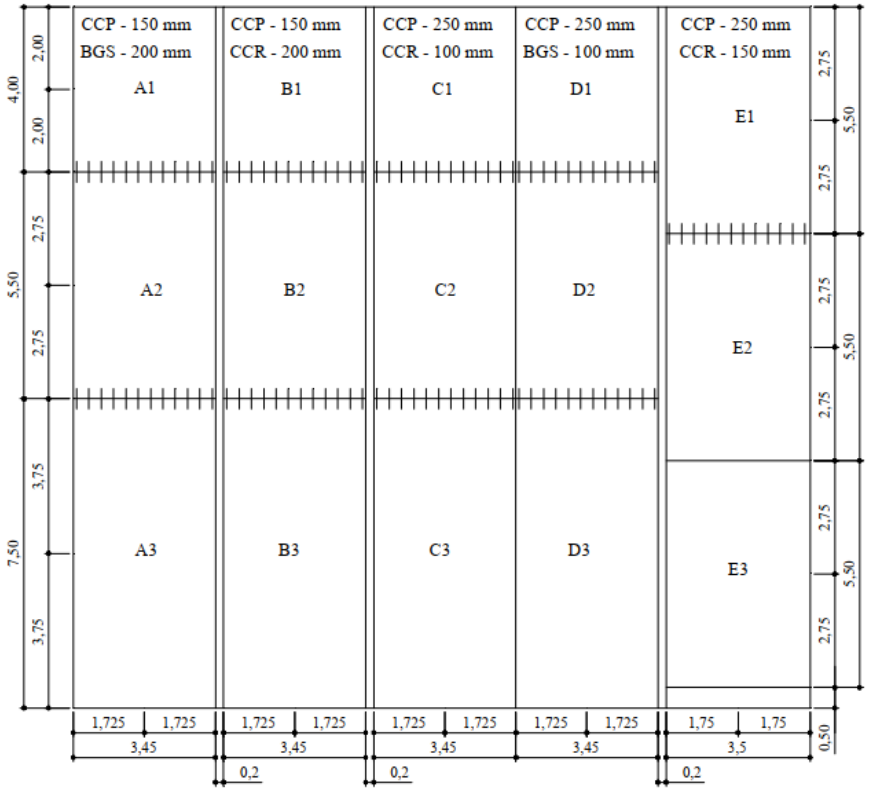

Source: Severi (2002)

Where CCP = thickness of the slab (h); BGS = used Simples Graded Gravel as material of subgrade; and CCR = used Roller-Compacted Concrete as material of subgrade.

Figure 4.22 – Position of the thermal resistors installed at experimental track at Polytechnic School of the University of São Paulo

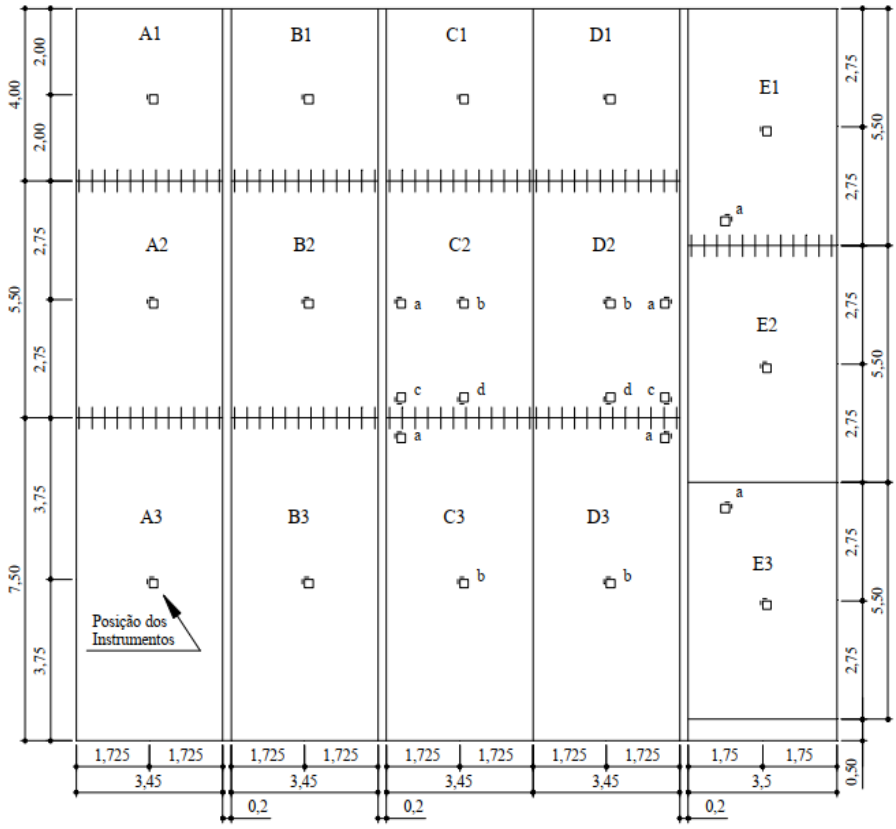

Source: Severi (2002)

Figure 4.23 - Temperature profile in a concrete slab for a day with Multiple Inversions. Graph constructed using Severi (2002)'s data. a) Profiles during the Day (6:00 to 18:00); b) Profiles during the Night (18:00 to 6:00)

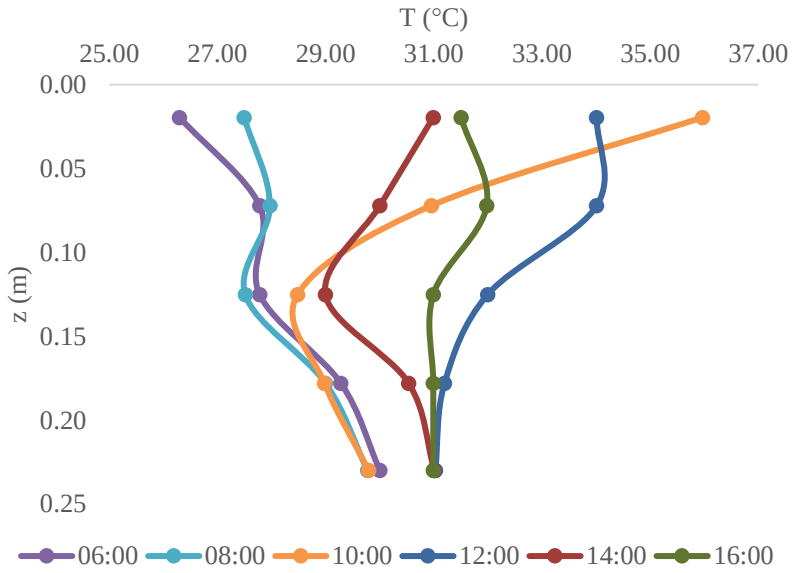

a)

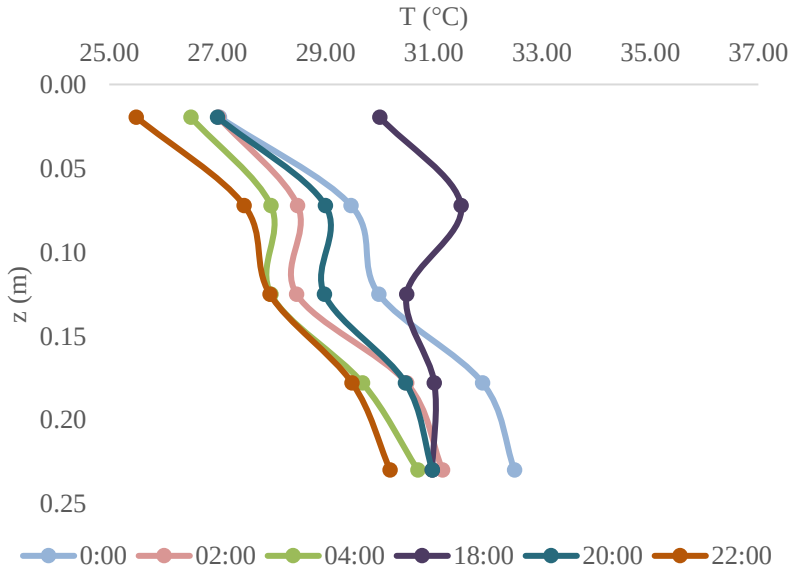

b)

Source: Author.

In order to know the values that describe the temperature profiles in concrete slabs in city of São Paulo, the Table 4.3 to Table 4.9 were created with the analysis of the temperature differential ($\Delta T = T_{top} - T_{bot}$) and the parameter proposed by Hiller and Roesler (2010) ($NOLA$). For each variable, its maximum, average, minimum values, standard deviation, 5th

percentile (Q05), 25th percentile (Q25), 50th percentile (or median), 75th percentile (Q75), 95th percentile (Q95), range between quartiles (IQR = Q75 – Q25), asymmetry and kurtosis were obtained. The data was separated into scenarios depending on the day and time collected: spring, summer, autumn, winter, day, night and total. All these tables were constructed by the author analyzing and organizing the Severi (2002)'s data.

Table 4.3 - Statistical parameters calculated from temperature measurements in São Paulo from data collected by Severi (2002) during spring.

	ΔT (°C)	$NOLA$ (°C m)
Maximum	14.901	0.280
Average	-0.092	-0.067
Minimum	-5.782	-0.671
Standard Deviation	4.916	0.203
Q05	-5.223	-0.456
Q25	-3.954	-0.175
Median	-2.016	-0.029
Q75	2.969	0.048
Q95	9.841	0.241
IQR	6.923	0.223
Asymmetry	1.088	-0.699
Kurtosis	0.313	0.154

Source: Author.

Table 4.4 - Statistical parameters calculated from temperature measurements in São Paulo from data collected by Severi (2002) during summer.

	ΔT (°C)	$NOLA$ (°C m)
Maximum	16.837	0.342
Average	0.407	-0.098
Minimum	-5.512	-0.504
Standard Deviation	5.297	0.194
Q05	-4.976	-0.433
Q25	-3.859	-0.277
Median	-1.239	-0.037
Q75	3.868	0.006
Q95	10.355	0.236
IQR	7.727	0.283
Asymmetry	1.137	-0.278
Kurtosis	0.695	-0.442

Source: Author.

Table 4.5 - Statistical parameters calculated from temperature measurements in São Paulo from data collected by Severi (2002) during autumn.

	ΔT (°C)	$NOLA$ (°C m)
Maximum	13.467	0.260
Average	2.377	0.080
Minimum	-1.439	-0.315
Standard Deviation	3.749	0.131
Q05	-0.961	-0.265
Q25	-0.494	0.051
Median	0.735	0.116
Q75	3.998	0.159
Q95	11.327	0.223
IQR	4.492	0.108
Asymmetry	1.304	-1.512
Kurtosis	0.939	1.885

Source: Author.

Table 4.6 - Statistical parameters calculated from temperature measurements in São Paulo from data collected by Severi (2002) during winter.

	ΔT (°C)	$NOLA$ (°C m)
Maximum	10.929	0.110
Average	0.318	-0.157
Minimum	-5.985	-0.667
Standard Deviation	4.311	0.192
Q05	-4.542	-0.528
Q25	-3.149	-0.249
Median	-0.612	-0.103
Q75	2.941	-0.015
Q95	9.394	0.076
IQR	6.090	0.234
Asymmetry	0.837	-0.910
Kurtosis	-0.224	-0.075

Source: Author.

Table 4.7 - Statistical parameters calculated from temperature measurements in São Paulo from data collected by Severi (2002) during day (from 6:00 AM to 6:00 PM).

	ΔT (°C)	$NOLA$ (°C m)
Maximum	16.837	0.342
Average	3.065	-0.178
Minimum	-5.985	-0.671
Standard Deviation	5.186	0.217
Q05	-4.790	-0.518
Q25	-1.202	-0.350
Median	2.989	-0.171
Q75	6.972	-0.038
Q95	11.544	0.173
IQR	8.173	0.312
Asymmetry	0.281	0.056
Kurtosis	-0.668	-0.605

Source: Author.

Table 4.8 - Statistical parameters calculated from temperature measurements in São Paulo from data collected by Severi (2002) during night (from 6:00 PM to 6:00 AM).

	ΔT (°C)	$NOLA$ (°C m)
Maximum	8.008	0.286
Average	-2.098	0.042
Minimum	-5.782	-0.214
Standard Deviation	2.411	0.102
Q05	-5.138	-0.131
Q25	-3.991	-0.020
Median	-2.729	0.020
Q75	-0.238	0.109
Q95	2.319	0.221
IQR	3.753	0.130
Asymmetry	0.855	0.284
Kurtosis	0.893	-0.377

Source: Author

Table 4.9 - Statistical parameters calculated from temperature measurements in São Paulo from data collected by Severi (2002)

	ΔT (°C)	$NOLA$ (°C m)
Maximum	16.837	0.342
Average	0.501	-0.069
Minimum	-5.985	-0.671
Standard Deviation	4.805	0.203
Q05	-4.976	-0.456
Q25	-3.403	-0.175
Median	-0.519	-0.024
Q75	3.059	0.065
Q95	9.885	0.213
IQR	6.462	0.240
Asymmetry	0.968	-0.679
Kurtosis	0.292	-0.025

Source: Author.

When analyzing the tables, it is possible to notice the values that describe the temperatures in the concrete slabs in São Paulo. The ΔT presented a maximum value on a summer day, a minimum on a winter day, an average of around 0.50°C, asymmetry to the right and a leptokurtic distribution. The $NOLA$ presented a maximum value on a summer day, a minimum on a spring day, an average of around -0.07, left asymmetry and a platykurtic, almost mesokurtic, distribution. Therefore, it is possible to notice that during summer or spring days the highest stresses occur and the lowest during winter days, however high stresses can occur in all seasons of the year.

In addition to the tables, Figure 4.24 to Figure 4.27 present the graphs constructed with the aim of verifying whether there was a relationship between the variables to the point of replacing the use of artificial intelligence, in addition to helping to understand the linear and self-equilibrating components existing in the stresses. Summer data was chosen, as it presented the highest stresses, and the entire data set was subsequently used. The graphs were organized according to the aircraft type (A380 and B747) and stress position (Top or Bottom). In the first column, are presented the stresses predicted using ΔT_{Q05} and $NOLA_{Q05}$ as input to top stress or ΔT_{Q95} and $NOLA_{Q05}$ as input to bottom stress, the alternation of these parameters is with the aim of presenting the highest stresses. The second and third columns show the stresses corresponding to each variable: ΔT (ΔT_{Q05} when top stress and ΔT_{Q95} when bottom stress) and $NOLA_{Q05}$ respectively. And the last one shows the characteristic stress, the 95th percentile of the total stresses presented in the São Paulos's slabs (σ_{Q95}), the choosing of theses parameters is with the aim of presenting the highest stresses. For all variables, linear and self-balancing stresses were calculated, in addition to showing the maximum (σ_{max}), average (σ_{mean}) and minimum (σ_{min}) total stresses of each scenario, considering the stresses that happened in this period, with all values divided by their respective linear stress generated when the temperature differential from the top to bottom of the slab are equal to zero ($\sigma_{\Delta T=0}$), as shown in Table 4.10. All stresses were obtained using the following parameters: h = 0.250m, LTE = 85%, ℓ = 1.32m e k = 13.6 MPa/m, selected to be the parameters presented in the database more similar to the conditions involved in the Severi (2002)'s data obtaining.

Table 4.10 – Linear stress for $\Delta T = 0$ ($\sigma_{\Delta T=0}$) for each configuration.

	B747	A380
Stress position	$\sigma_{\Delta T=0}$ (MPa)	$\sigma_{\Delta T=0}$ (MPa)
Top	2.225	2.630
Bottom	6.617	4.490

Source: Author.

Figure 4.24 - Stress graph generated from São Paulo summer temperature data for A380, h = 0.250m, LTE = 85%, ℓ = 1.32m, k = 13.6 MPa/m. a) Top stress; b) Bottom stress

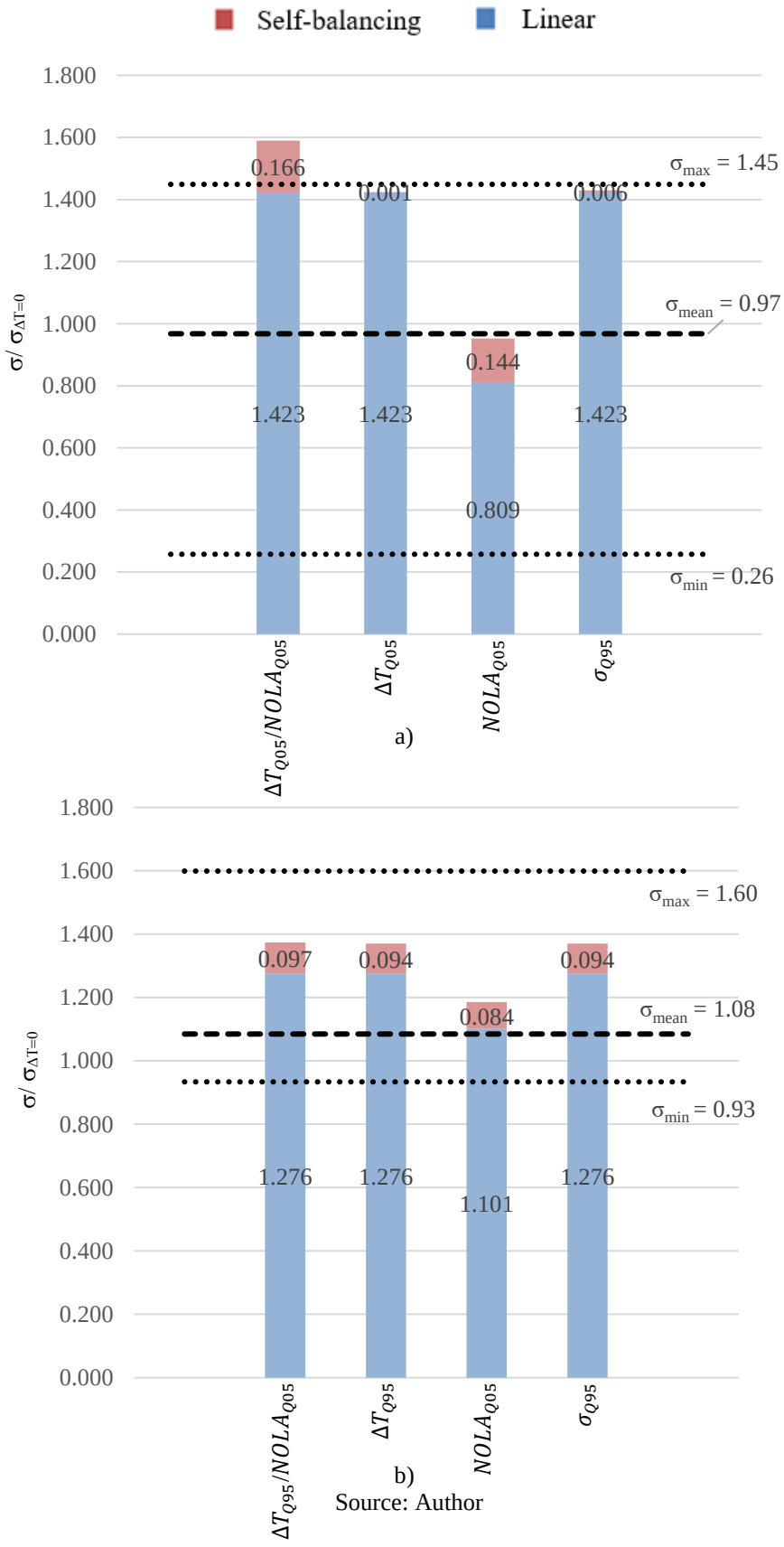

Source: Author

Figure 4.25 - Stress graph generated from São Paulo summer temperature data for B747, h = 0.250m, LTE = 85%, ℓ = 1.32m, k = 13.6 MPa/m. a) Top stress; b) Bottom stress

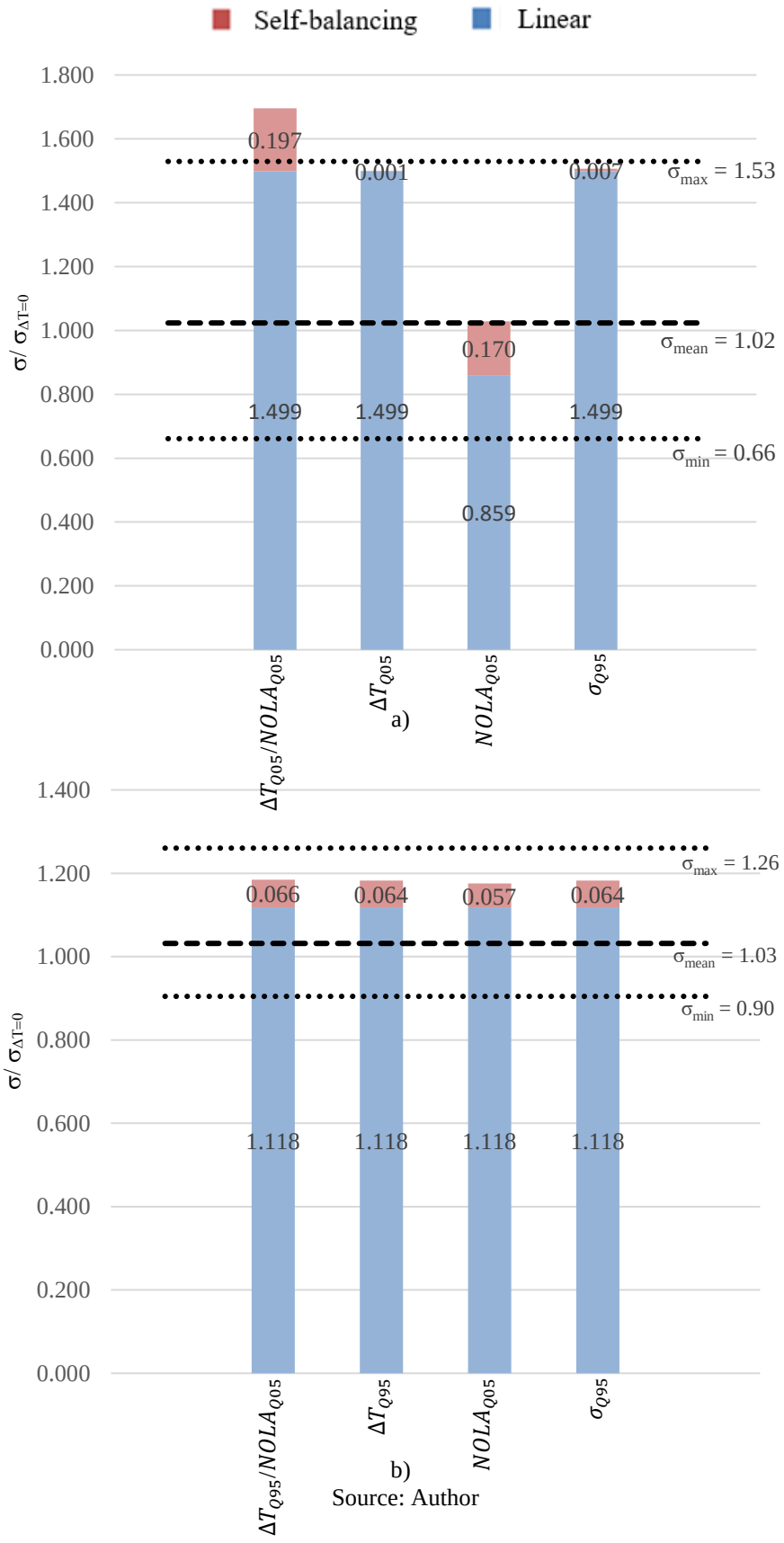

Source: Author

Figure 4.26 – Stress graph generated from all temperature data from São Paulo for A380, h = 0.250m, LTE = 85%, ℓ = 1.32m, k = 13.6 MPa/m. a) Top stress; b) Bottom stress

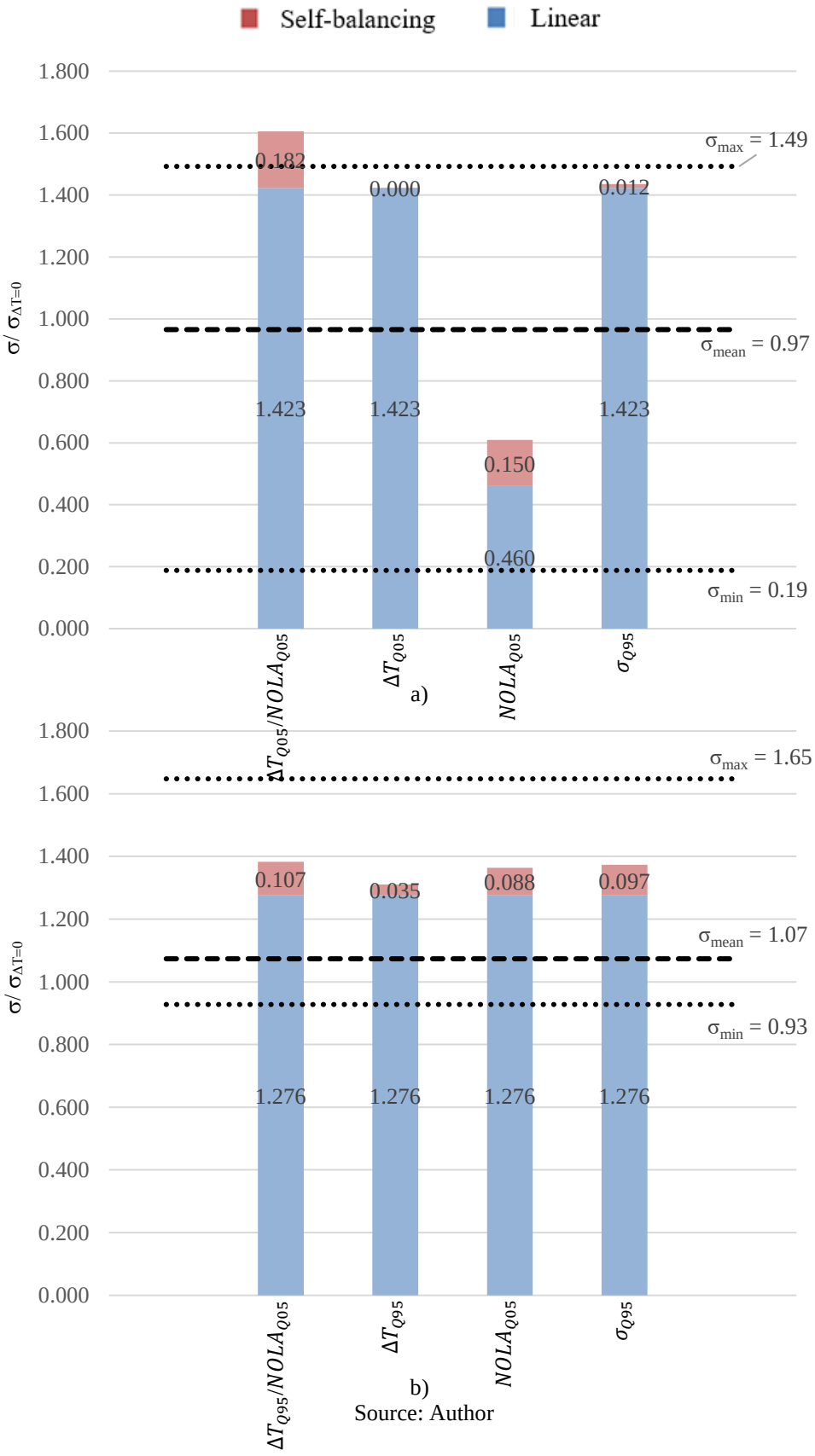

Source: Author

Figure 4.27 - Stress graph generated from all temperature data from São Paulo for B747, h = 0.250m, LTE = 85%, ℓ = 1.32m, k = 13.6 MPa/m. a) Top stress; b) Bottom stress

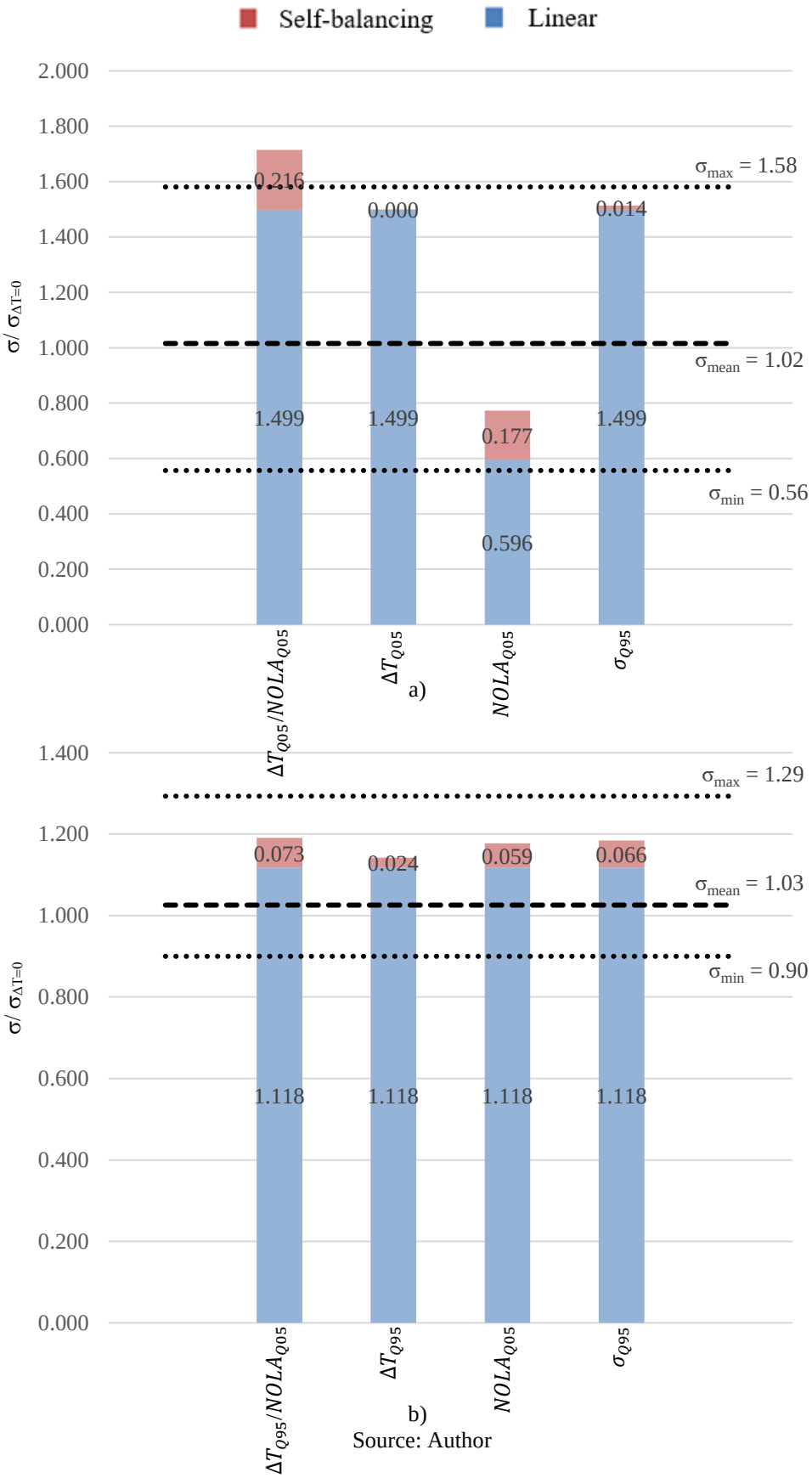

Source: Author

Analyzing the graphs, relationships between the variables were found, with ΔT_{Q95} or ΔT_{Q05} being sufficient to determine the linear stresses arising from σ_{Q95}. Furthermore, it was possible to better understand the behavior of stresses and confirm the importance of analyzing the temperatures involved, as, in some cases, there is the possibility of increasing by more than 50% or decreasing by more than 40% the stresses acting on concrete pavements.

5. CONCLUSION

The proposed machine learning models based on eleven input variables including type of aircraft (B747 and A380), geometry, loading and material properties, was able to very accurately predict the maximum top and bottom tensile stresses due to the landing gear and temperature differentials, obtaining an MSE equal to 3.60e-4 MPa^2 to the test dataset. This was possible due to the structure of the optimized random forest algorithm which used decision trees, that in the case of the dataset in this paper, was able to be efficiently trained to substitute computationally cost finite element analysis involving mechanical and temperature loadings and predict stresses in seconds without the necessity of rebuilding a model. The analysis of the absolute errors showed that, even for the testing dataset, those errors were smaller than 0.20MPa in the majority of the cases, only presenting three errors greater than that, but smaller than 0.25MPa, showing high accuracy and reliability. In addition of this, the histogram of absolute residuals shows the highest concentration around 0MPa. In this way, machine learning models can be trained using a broad database from responses previously modeled by the finite element method to create a generalizing model that accurately predicts the tensile stress results and no longer requires the use of costly analyzes with that numerical method.

5.1. SUGGESTIONS OF FUTURE WORKS

Despite the excellent results presented by the proposed model, there are still points that can be improved in order to further increase its predictive power. Therefore, the following proposals for future works are made:

- Use finite element models and create a database with a greater diversity of values in each variable;
- To train and validate a new Random Forest model using a database with a greater diversity of inputs;

- Submit the model proposed by this work and check its performance using values different from those existing in the database used;
- Carry out temperature studies on concrete slabs in regions outside São Paulo.

REFERENCES

An Introduction to Gradient Boosting Decision Trees. **Machine Learning Plus**, 2024. Available in: https://www.machinelearningplus.com/machine-learning/an-introduction-to-gradient-boosting-decision-trees/. Accessed in: 29 dec, 2024.

BALBO, J. T. **Pavimentos de concreto**. 1st ed. São Paulo, Brazil: Oficina de textos, 2009.

BALBO, J. T. and SEVERI, A. A. **Thermal gradients in concrete pavements in tropical environment experimental appraisal**. *Transportation Research Record*, vol. 1809, no. 1, pp. 12-22, 2002.

BRADBURY, R. D. **Reinforced concrete pavements**. 1st ed. Washington, D.C., United States of America: Wire Reinforcement Institute, 1938.

CHOUBANE, B. and TIA, M. **Nonlinear temperature gradient effect on maximum warping stresses in rigid pavements**. *Transportation Research Record*, no. 1370, pp. 11-19, 1992.

CHOUBANE, B. and TIA, M. **Analysis and verification of thermal-gradient effects on concrete pavements**. *Journal of Transportation Engineering, ASCE*, vol. 121, no. 1, pp. 75-81, 1995.

DAVIDS, W. G.; TURKIYYAH G. M. and MAHONEY, J. P. ***EverFE* rigid pavement three-dimensional finite element analysis tool**. *Transportation Research Record*, vol. 1629, no. 1, pp. 41-49, 1998.

DUCLOS, F. Asiana Airlines: L'airbus A380 Tout Beau Tout Neuf. **Air Journal**, 28 mar 2014. Actualité. Available in: https://www.air-journal.fr/2014-03-28-asiana-airlines-lairbus-a380-tout-beau-tout-neuf-5102791.html. Accessed in: 29 dec, 2024.

FAA - Federal Aviation Administration. **Airport pavement design and evaluation**. Advisory Circular (AC) 150/5320-6F, FAA, Washington-DC, 2016.

FAA - Federal Aviation Administration. **Airport pavement design and evaluation**. Advisory Circular (AC) 150/5320-6E, FAA, Washington-DC, 2009a.

FAA - Federal Aviation Administration. **Calibration of FAARFIELD rigid pavement design procedure**. DOT/FAA/AR-09/57, FAA, Washington, DC, 2009b.

FAA - Federal Aviation Administration. **Advanced pavement design: finite element modeling for rigid pavement joints. Report ii – model development**. DOT/FAA/AR-97/7, FAA, Washington, DC, 1997a.

FAA - Federal Aviation Administration. **Development of advanced computational models for airport pavement design**. DOT/FAA/AR-97/47, FAA, Washington, DC, 1997b.

FONTELES, D. A. **Análise de tensões em pavimentos rígidos aeroportuários submetidos a cargas mecânicas e cargas térmicas sazonais não lineares**. Dissertação de Mestrado em

Estruturas e Construção Civil. Publicação E.TD-18A/17, Departamento de Engenharia Civil e Ambiental, Universidade de Brasília, Brasília, DF, 120 p., 2017.

GUNGOR, O. E. and AL-QADI, I. L. **Developing machine learning models to predict airfield pavements responses**. *Transportation Research Record*, vol. 2672, no. 29, pp. 23-34, 2018.

HILLER, J. E. **Development of mechanistic-empirical principles for jointed plain concrete pavement fatigue design**. Ph.D. dissertation, Civil Environmental Engineering, University of Illinois, Urbana-Champaign, Illinois, United States of America, 2007.

HILLER, J. E. and ROESLER, J. R. **Simplified nonlinear temperature curling analysis for jointed concrete pavements**. *Journal of Transportation Engineering, ASCE*. vol. 136, no. 7, pp. 654-663, 2010.

HILLER, J. E. and ROESLER, J. R. **Transverse joint analysis for mechanistic-empirical design of rigid pavements**. *Transportation Research Record*, vol. 1809, no. 1, pp. 42-51, 2002.

HUANG, Y. H. **Pavement analysis and design**. 2nd ed. New Jersey, USA: Pearson, 2003.

HUANG, Y. H and WANG S. T. **Finite element analysis of rigid pavements with partial subgrade contact**. *Transportation Research Record*, vol. 485, pp. 39-54, 1974.

HUANG, Y. H. **Critical tensile strain in asphalt pavements**. *Transportation Engineering Journal of ASCE,* Vol. 99, No. 3, pp. 553-569, 1973.

IOANNIDES, A. M. and KHAZANOVICH, L. **Nonlinear temperature effects on multilayered concrete pavements**. *Journal of Transportation Engineering, ASCE*, vol. 124, no. 2, pp. 128-136, 1998.

JUNG, D.; LEE, J.; BAEK, C.; AN, D. and YANG, S. **Predicting concrete pavements condition for sustainable management: unveiling the development of distresses through machine learning**. *Sustainability*, vol. 16, no. 2, pp. 573, 2024.

KAWSAR, A.; SEKER, NHM K. and AFSANA, S. **Artificial intelligence-based approaches to predict concrete compressive strength**. 7^{th} *International Conference on Civil Engineering for Sustainable Development (ICCESD)*, 2024.

KHAZANOVICH, L. **Structural analysis of multi-layered concrete pavement systems**. Ph.D. dissertation, Civil Environmental Engineering, University of Illinois, Urbana-Champaign, Illinois, United States of America, 1994.

KHAZANOVICH, L. e IOANNIDES, A. M. **Structural analysis of unbonded concrete overlays under wheel and environmental loads**. *Transportation Research Record*, vol. 1449, pp. 174-181, 1994.

KOROVESIS, G. T. **Analysis of slab-on-grade pavements system subjected to wheel and temperature loading**. Ph.D. dissertation, Civil Environmental Engineering, University of

Illinois, Urbana-Champaign, Illinois, United States of America, 1990.

MELOSH, R. J. **Basis for derivation of matrices for the direct stiffness method**. *Journal of the AIAA*, vol. 1, no. 7, pp. 1631-1637, 1963.

MOHAMED, A. R. and HANSEN, W. **Effect of nonlinear temperature gradient on curling stress in concrete pavement**. *Transportation Research Record*, vol. 1568, no. 1, pp. 65-71, 1997.

MORETTIN, P. A. and SINGER, J. M. **Estatística e ciência de dados**. 1st ed. Rio de Janeiro, Rio de Janeiro, Brazil: LPC, 2022.

MUELLER, T; KUSNE, A. G. and RAMPRASAD, R. **Machine learning in materials science: recent progress and emerging applications**. in *Reviews in Computational Chemistry*, Parrill, A. L. and Lipkowitz, K. B. vol. 29, Hoboken, New Jersey, United States of America: Wiley, 2016, ch. 4, pp. 186-273, 2016.

PASUPUNURI, S. K.; THOM, N. and LI, L. **Use of machine learning algorithms for predicting the transverse cracking in jointed plain concrete pavements**. *American Society of Civil Engineers, ASCE, Airfield and Highway Pavements 2023*, pp. 172 – 184, 2023.

RODDEN, R. **Analytical modeling of environmental stresses in concrete slabs**. M.S. thesis, Civil Environmental Engineering, University of Illinois, Urbana-Champaign, Illinois, United States of America, 2006.

RUFINO, D. and ROESLER, J. R. **Effects of temperature curling on airfield rigid pavement responses**. *Road Materials and Pavement Design*, vol. 6, no. 3, pp. 311-337, 2005.

SAVIETTO, J. V. Machine Learning: Métricas, Validação Cruzada, Bias e Variância. **Medium**, 2021. Available in: https://medium.com/@jvsavietto6/machine-learning-m%C3%A9tricas-valida%C3%A7%C3%A3o-cruzada-bias-e-vari%C3%A2ncia-380513d97c95. Accessed in: 29 dec, 2024.

SEVERI, A. A. **Estudo dos gradientes térmicos em pavimentos de concreto de cimento portland no ambiente tropical**. Ph.D. dissertation. Transportation Engineering, University of São Paulo, São Paulo, SP, Brazil, 2002.

SULIMAN, A. M.; AWED, A. M.; ABD EL-HAKIM, R. T. A. and EL-BADAWY, S. M. **International roughness index prediction for jointed plain concrete pavements using regression and machine learning techniques**. *Transportation Research Record*, vol. 2678, no. 2, pp. 235-250, 2024.

TABATABAIE, A. M. **Structural analysis of concrete pavement systems**. *Transportation Engineering Journal of ASCE*, vol. 106, no. 5, pp. 493-506, 1980.

TABATABAIE, A. M. and BARENBERG, E. J. **Finite-element analysis of jointed or cracked concrete pavements**. *Transportation Research Record*, vol. 671, no. 3, pp. 11-19, 1978.

THOMLINSON, J. **Temperature variations and consequent stresses produced by daily and seasonal temperature cycles in concrete slabs**. *Concrete Constructional Engineering*, London, U. K., vol. 36, no. 6, pp. 298-307, 1940.

THOMPSON, M. R. and BARENBERG, E. J. **Calibrated mechanistic structural analysis procedure for pavements**. *National Cooperative Highway Research Program*, vol.1, 1992.

TIA, M.; ARMAGHANI, J. M.; WU, C. L.; LEI, S. and TOYE, K. L. **FEACONS III computer program for an analysis of jointed concrete pavements**. *Transportation Research Record*, vol. 1136, pp. 12-22, 1987.

WESTERGAARD, H. M. **Analysis of stresses in concrete pavements due to variations of temperature**. *Highway Research Board*, vol. 6, pp. 201-215, 1927.

WESTERGAARD, H. M. **Stresses in concrete pavement computed by theoretical analysis**. *Federal Highway Administration*, vol. 7, no. 2, pp. 25-35, 1926.

APPENDIX A - TEMPERATURE PROFILES IN CONCRETE SLABS IN THE CITY OF SÃO PAULO FOR DIFFERENT WEATHER CONDITIONS

All the graphs in this appendix were done by the author based on the measurements collected and presented in Severi (2002).

Figure A.1 – Temperature profiles along the depth of the concrete slab in the city of São Paulo: a) Spring 1 – 12/06/2000; b) Spring 2 – 12/07/2000; c) Spring 3 – 08/12/2000; d) Primera 4 – 12/09/2000; e) Rainy Day – 12/01/2000; f) Multiple Inversion – 12/10/2000

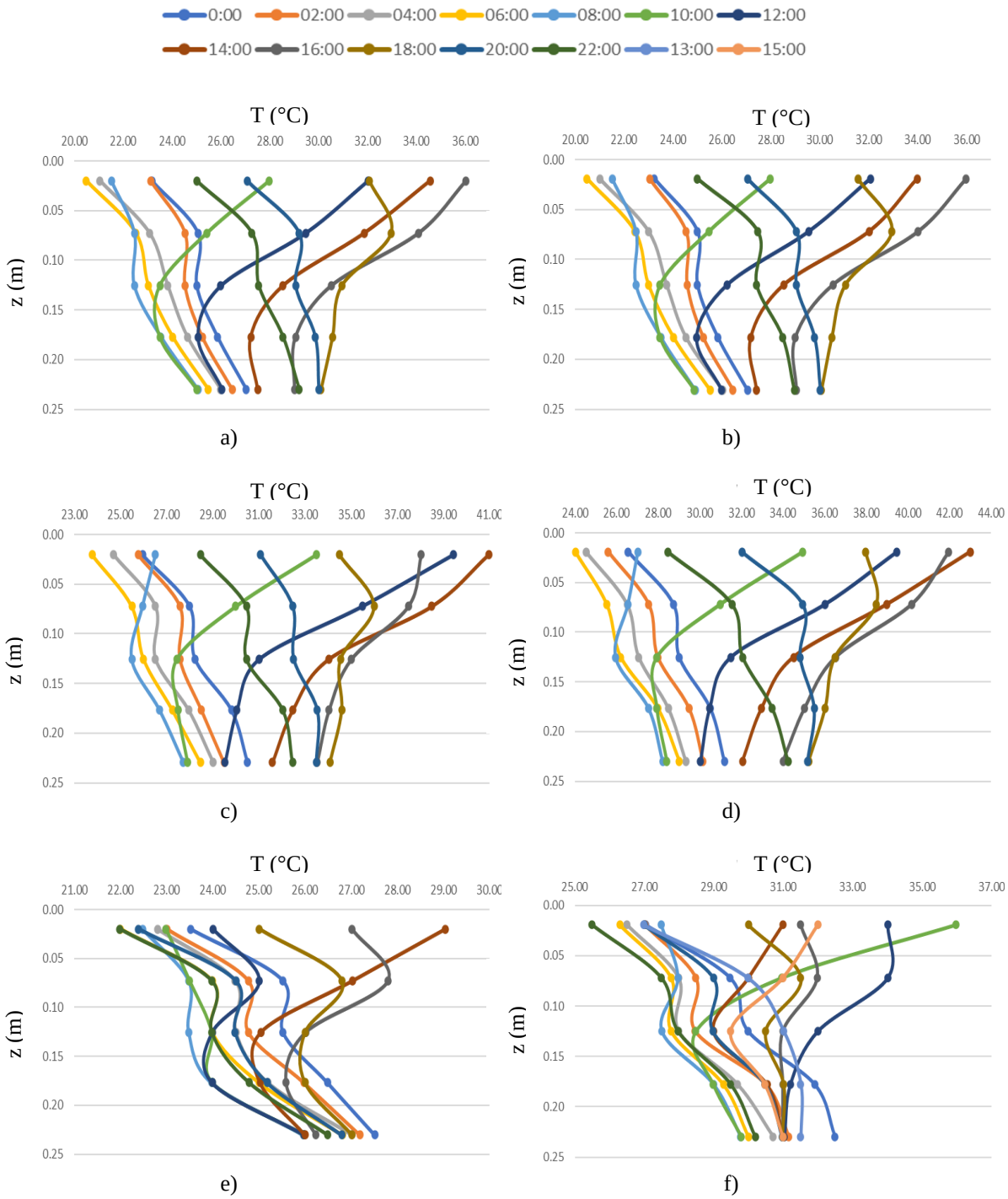

Source: Author.

Figure A.2 - Temperature profiles along the depth of the concrete slab in the city of São Paulo: a) Summer 1 – 10/02/2001; b) Summer 2 – 11/02/2001; c) Summer 3 – 12/02/2001; d) Summer 4 – 13/02/2001; e) Hot sunny day – 08/02/2001; f) Typical situation – 11/12/2000

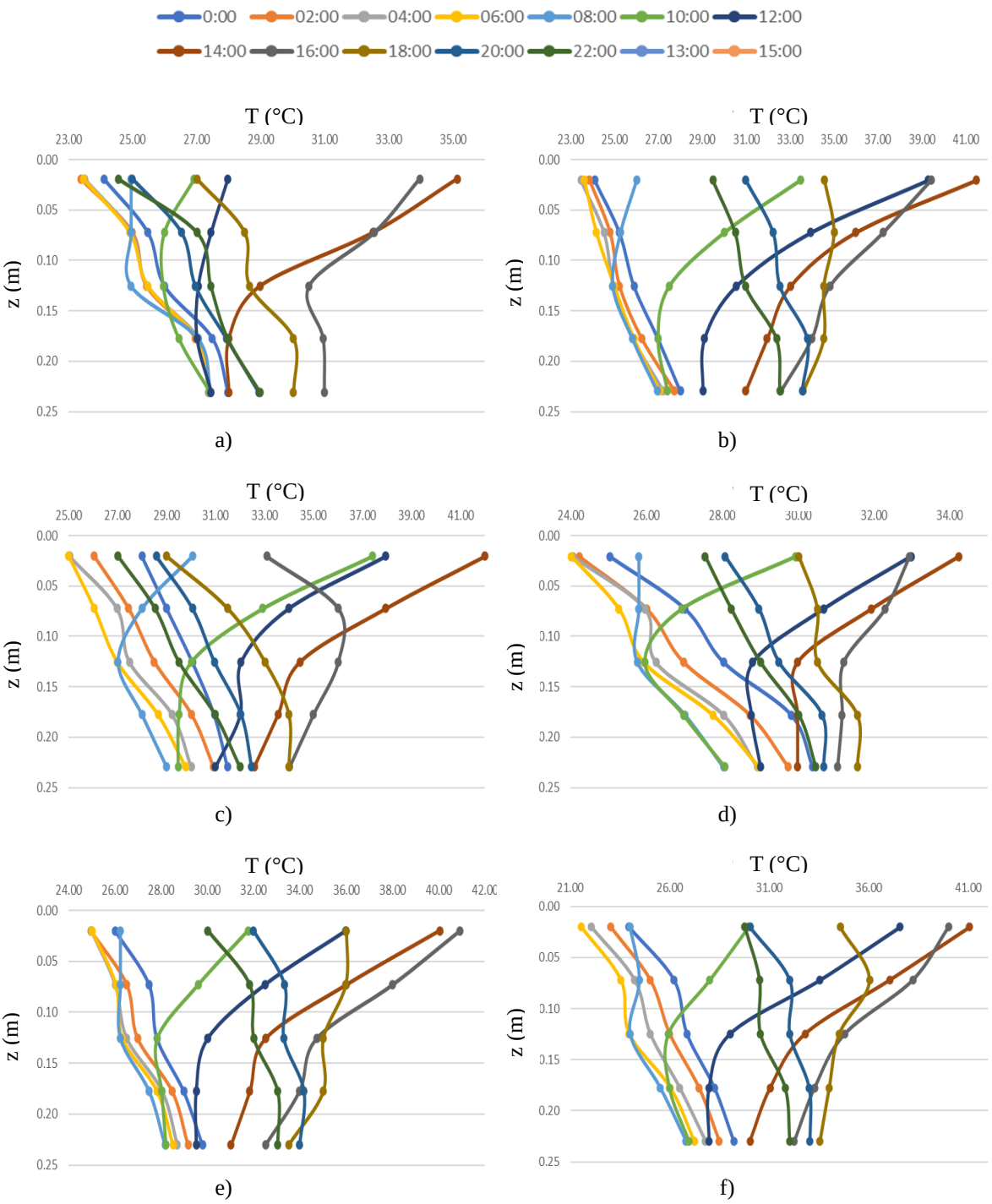

Source: Author.

Figure A.3 - Temperature profiles along the depth of the concrete slab in the city of São Paulo: a) Autumn 1 – 21/03/2000; b) Autumn 2 – 03/22/2000; c) Autumn 3 – 03/23/2000; d) Autumn 4 – 03/24/2000; e) Positive thermal differential all day – 10/17/2000; f) Negative thermal differential all day – 11/14/2000

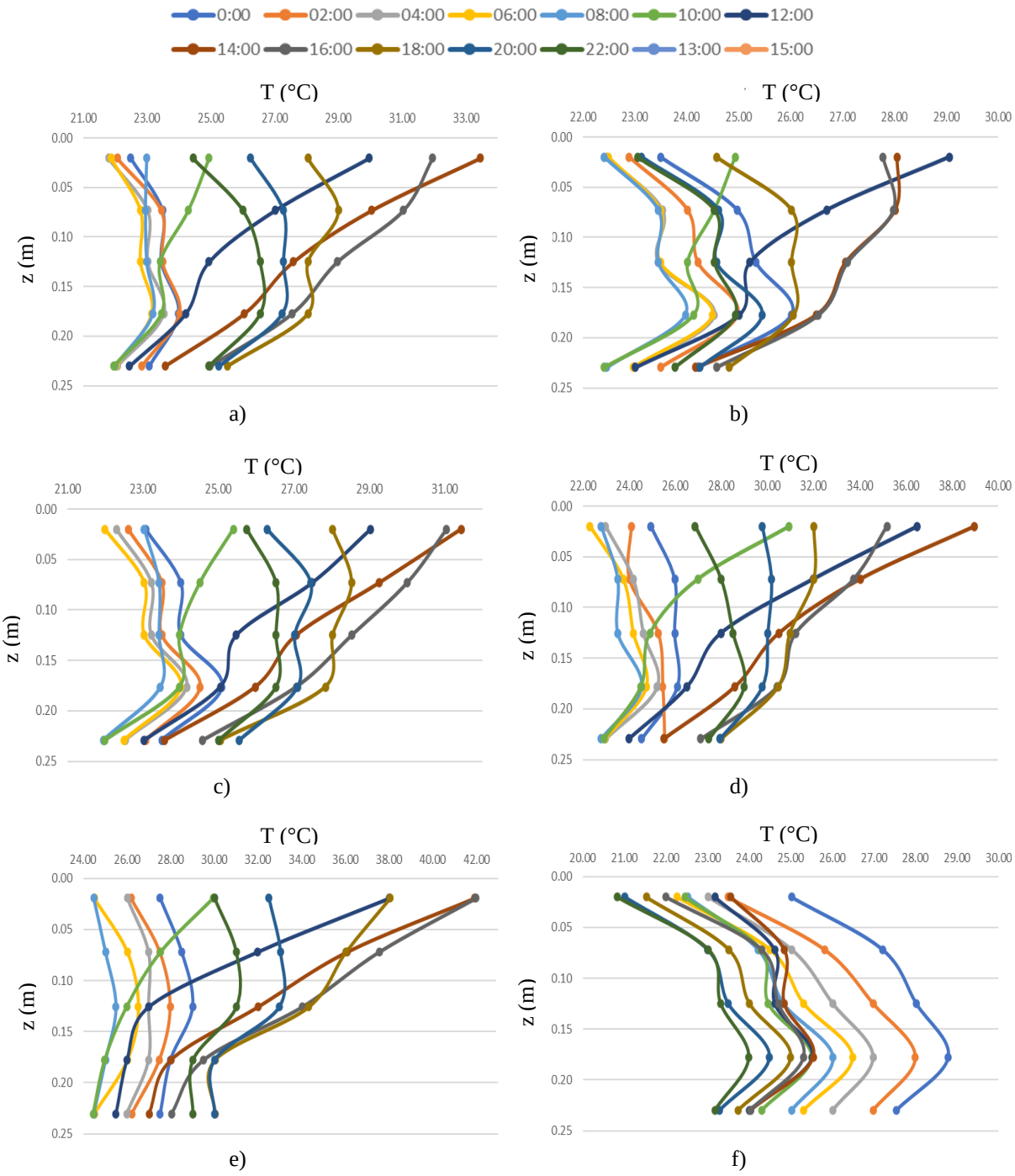

Source: Author.

Figure A.4 - Temperature profiles along the depth of the concrete slab in the city of São Paulo: a) Winter 1 – 09/08/2000; b) Winter 2 – 09/09/2000; c) Winter 3 – 10/09/2000; d) Winter 4 – 11/09/2000; e) Cloudy Day 1 – 12/09/1999; f) Cloudy Day 2 – 07/03/2000

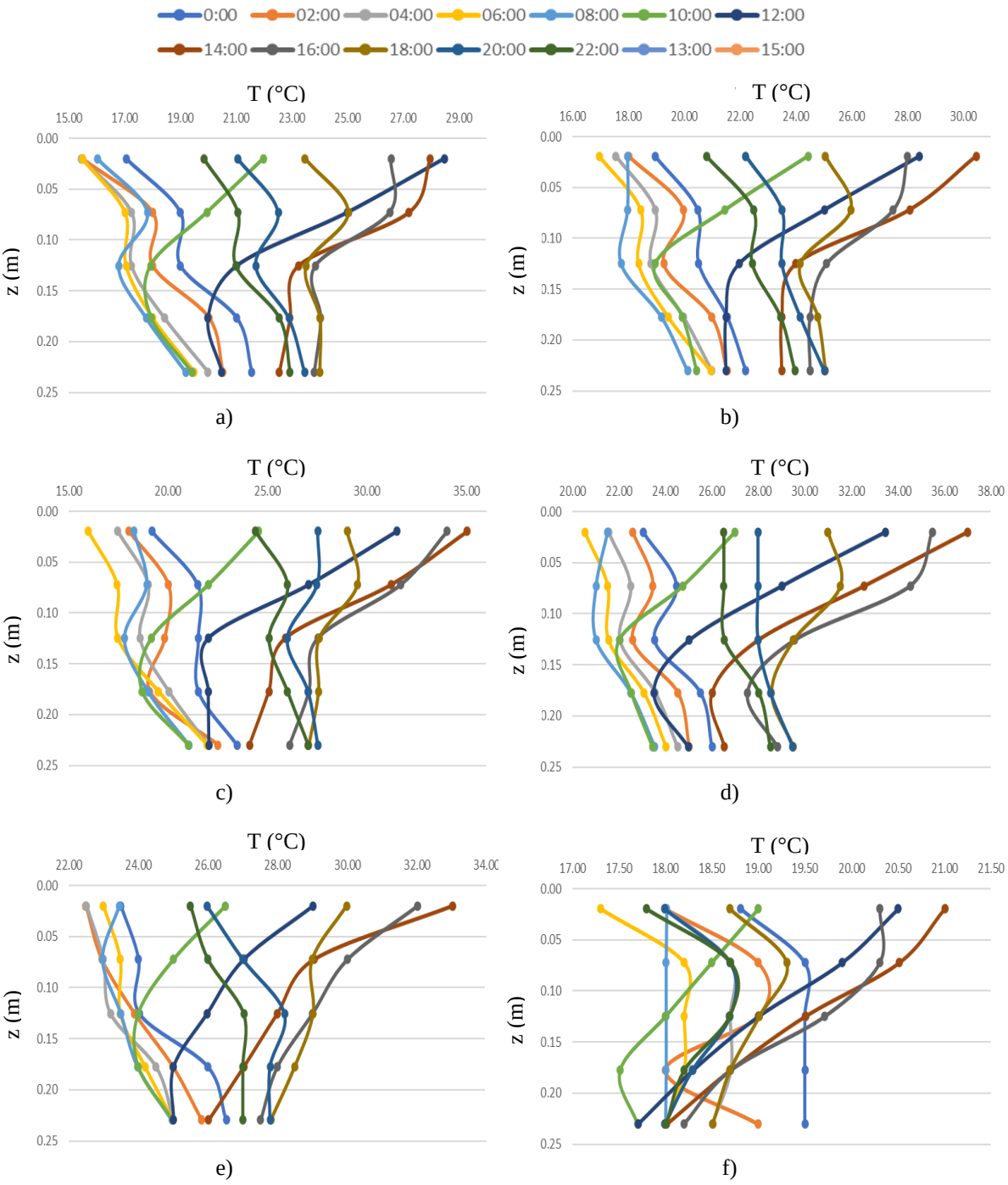

Source: Author.